8-2017

Analysis of the Hite Fault Group, Southeast Utah: Insights into Fluid Flow Properties in a Reservoir Analog

Daniel J. Curtis
Utah State University

Recommended Citation

ANALYSIS OF THE HITE FAULT GROUP, SOUTHEAST UTAH: INSIGHTS INTO

FLUID FLOW PROPERTIES IN A RESERVOIR ANALOG

by

Daniel J. Curtis

A thesis submitted in partial fulfillment

of the requirements for the degree

of

MASTER OF SCIENCE

in

Geology

Approved:

_____   _____
James P. Evans, Ph.D.   Kelly Bradbury, Ph.D.
Major Professor   Committee Member

_____   _____
Elizabeth Petrie, Ph.D.   Mark R. McLellan, Ph.D.
Committee Member   Vice President for Research and
                                                Dean of the School of Graduate Studies

UTAH STATE UNIVERSITY
Logan, Utah

2017

ABSTRACT

Analysis of the Hite Fault Group, Southeast Utah: Insights into Fluid Flow Properties in a

Reservoir Analog

by

Daniel J. Curtis, Master of Science

Utah State University, 2017

Major Professor: Dr. James P. Evans
Department: Geology

Faults in porous sandstones are typically thought of as low permeability systems, but deformation band faults in some areas may act as fluid pathways or as barriers to fluid flow. In a massive sandstone (erg-type) reservoir setting such as the Cedar Mesa Sandstone it is essential to understand how different structures might affect porosity and permeability. Studying the faults, fractures, and associated damage zones present in these reservoirs allows for a better understanding of potential migration pathways within the petroleum system and provides useful information for the oil and gas industry.

We examine three mesoscale (cm- to m- scale) normal faults that are part of the Hite Fault Group in the Cedar Mesa Sandstone, Southeast Utah. The analysis of these three faults gives insight into the effects that small-scale normal faults and their associated damage zones can have one the porosity and permeability of an erg-type reservoir. Whole-rock geochemistry, mineralogy, permeability measurements, petrography, ultraviolet photography, and outcrop observations were used to attain

insights into cross-cutting relationships, past fluid compositions, and fault characteristics. These data show evidence for multiple fluid flow events.

We describe the fault paragenesis, which allows us to show that grain and bed scale fractures as well as small faults are features by which fluids can migrate preferentially. We propose two separate events of slip that are each associated with a fluid flow event. An initial movement with a component of shear caused cataclasis and is expressed as deformation bands. This first event has an associated iron oxide rich fluid composition that mineralized in and around the fractures. Evidence for this mineralization is seen as fracture infillings as well as alteration halos. The second event is a reactivation of the faults resulting in an extensional episode that is accompanied by calcium rich fluid flow. In this event the faults are reactivated and open mode fractures are formed and subsequently mineralized by calcite.

(104 pages)

PUBLIC ABSTRACT

Analysis of the Hite Fault Group, Southeast Utah: Insights into Fluid Flow Properties in a

Reservoir Analogy

Daniel J. Curtis

In the subsurface faults can act as both barriers and conduits for fluids or gases

such as CO_2, hydrocarbons, or water. It is often thought that faults in porous rocks such as

sandstone are barriers to fluid flow. In this study we show that this is not always the case.

In sandstones like the Cedar Mesa Sandstone it is very important to understand the

relationships between this history of fault slip and fluid flow. Better understanding of

how fluids migrate through faults and the damaged areas surrounding these faults has

strong significance to the oil and gas industry.

In this study we examine a group of faults and their surrounding damage zones

near Hite, Utah. We analyze three of these small-scale faults in more detail. In doing so

we give insights into how these faults and their damage zones can effect fluid migration

as well as the porosity and permeability in the Cedar Mesa Sandstone. Whole rock

geochemistry, X-ray diffraction mineralogy, permeability data, petrography, ultraviolet

photography, and outcrop observations were used to gain insights into cross-cutting

relationships, past fluid compositions, and fault characteristics.

From the data that was collected from these faults we have begun to describe a

series of structural and fluid flow events. This series allows us to say that small-scale

faults and fractures are features by which fluids can migrate preferentially. In this series

of events we isolate two separate phases of movement. The first phase of movement

being has a component of shear in which the edges of the fractures are not moving directly apart. This event is accompanied by a fluid flow event the emplaced iron oxide in the fractures and the surrounding formation. The second event is a phase when the faults become reactivated by a stress that created open mode fractures. This second is accompanied by a fluid flow event that has high calcium content and emplaces calcite in the fractures. Throughout this study we give evidence to support this series of movement and fluid events.

ACKNOWLEDGMENTS

CONTENTS

LIST OF TABLES

LIST OF FIGURES

CHAPTER I

INTRODUCTION

1.1 Overview

Two major parts of a conventional petroleum system are the reservoir and

migration pathways that provide the conduits for the expulsion of fluids from a source

rock into the reservoir (Magoon and Dow, 1994). Faults in porous sandstones are

typically thought to be low permeability systems (Antonellini and Aydin, 1994), but

faults in these areas may also act as conduit pathways or as barriers to fluid flow (Beitler

et al., 2004; Beitler et al., 2005; Dockrill and Shipton; 2010, Fossen et al., 2007; Petrie et

al., 2013). In this study we investigate faults in the Cedar Mesa Sandstone, a

Pennsylvanian erg sequence of rocks located in southeastern Utah (Loope, 1984) to

examine the nature of small faults and their relationships to evidence of paleo fluid flow.

In the field area near Hite crossing on the Colorado River, southeastern Utah, the Cedar

Mesa Sandstone is cut by a series of small-scale, high angle normal faults that are herein

referred to as the Hite Fault Group. These faults can be seen on the geologic map (Figure

1). This series of small-scale normal faults that cuts and their associated damage zones

are the main focus of this study. We also see two main types of fractures in the study area

that are roughly parallel to the fault system. The first type is an open mode fracture and

the second is a fracture with a sense of shear movement. These two fracture types are

mineralized with calcite and/or iron oxide and occur near faults in the study area. In this

study faults will be divided into three zones: 1) protolith, 2) damage zone, and 3) fault
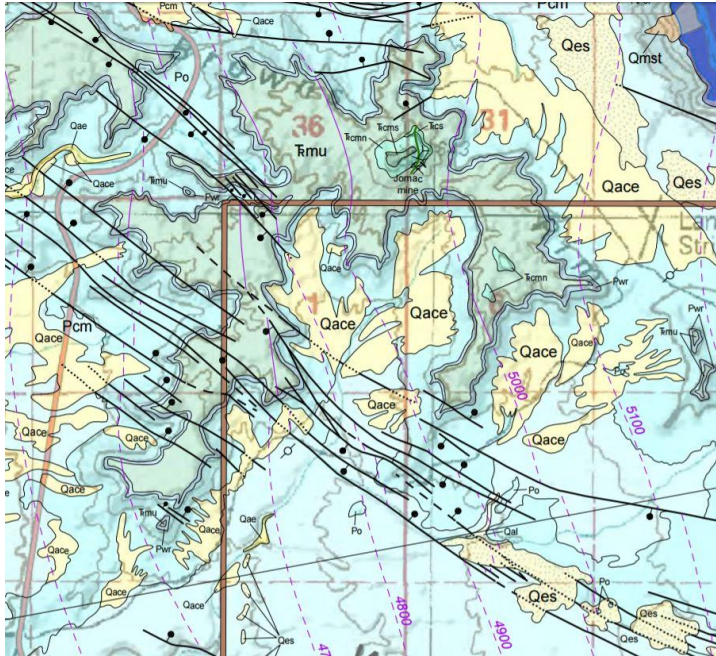
Figure 1. Hite Fault Group overview. This figure shows a geologic map that encompasses the Hite field are and shows the series of normal faults that is referred to at the Hite Fault Group in this study. The brown outline shows the old boundary between Glen Canyon National Recreation Area to the north and west and what now is Bear Ears National Monument but was previously BLM land during the time of the study to the south and east (Willis, 2012).

surface/core. These areas are chosen based on fracture density and fault slip surface outcrop.

Understanding permeability, fracture densities and distributions, and characteristics of the host rock that these faults and damage zones lie within is essential to understanding subsurface fluid flow in this area. In a massive sandstone (erg-type) reservoir setting such as the Cedar Mesa Sandstone (Huntoon et al., 2003), it is essential to understand how different structures might affect porosity and permeability. Petrie et al. (2013) showed that these faults exhibit evidence for low permeability that have been

reactivated. Fluids are then using these reactivated faults as conduits for flow. Fault

damage zones and structural diagenesis appear to have had variable effects on porosity

and permeability of the reservoir rock (Caine et al., 1996; Shipton et al., 2002; Davatzes

et al., 2005; Laubach et al., 2010).
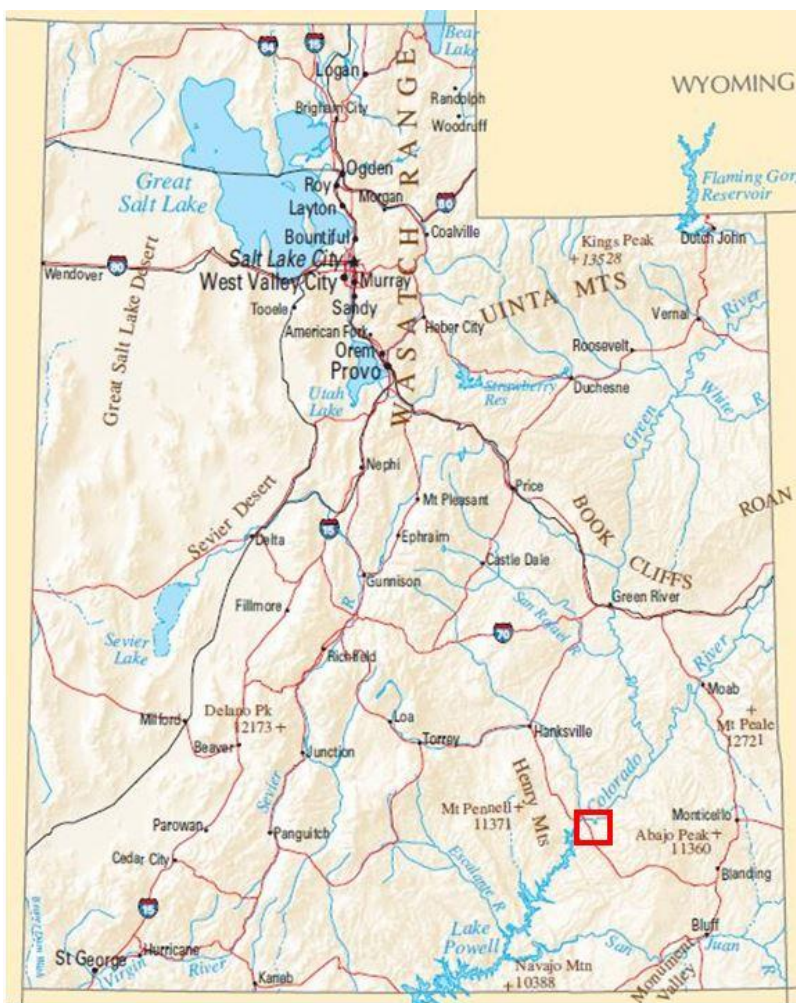
Figure 2. Hite Field Area location. Modified from the National Atlas of the United States
of America, Utah map 2004. Outlined in red is the Hite field area. Figure 1 displays the
geologic map which falls within this outlined area.

1.2 Objectives

Damage zones associated with faults can cause significant changes in the reservoir properties such as porosity and permeability (Caine et al., 1996; Shipton et al., 2002; Davatzes et al., 2005; Petrie et al., 2013). Deformation may increase or decrease flow pathways due to structural diagenesis and or brittle deformation (Laubach et al., 2010). Deformation and structural diagenesis will be characterized in order to test our hypothesis that grain and bed scale fractures as well as small faults are features by which fluids can migrate preferentially.

In this project we examine the deformation history of the Permian Cedar Mesa Sandstone, southeastern Utah (Loope, 1984; Langford and Chan, 1988; Stanesco and Campbell, 1989). We examine in detail the nature of fault damage zones associated with small-displacement normal faults within this rock unit in the Hite Fault Group. In each damage zone we measured fracture distributions, fracture densities, orientations, and offset of the faults. We identified evidence for paleo fluid flow within the damage zones. This evidence was gathered from mapping structural characteristics and associated features. These associated features include mineralization of fractures, staining of host rock in the immediate area surrounding fractures, and presence of fluorescent minerals under ultra violet light.

The specific study objectives are to: 1) Determine the history of how the faults formed in the Cedar Mesa Sandstone; 2) Characterize the extent to which the fault damage zones have caused alterations to reservoir porosity; and 3) Measure distribution data, fault orientation and distributions, and information pertaining to the mineralization

of the faults and fractures for input into various geostatistical and geometric models (Evans and Petrie, 2012).

The overall goal of this research effort was to provide data that can constrain the development of 3D fracture models for fluid flow simulations within the Cedar Mesa Sandstone reservoir. A model of this type should help to show that fault damage zones can cause changes in the permeability and porosity within the reservoir rock (Caine et al., 1996; Shipton et al., 2002; and Petrie et al., 2013). Data collected aim to test the hypothesis that grain and bed scale fractures as well as small faults are features by which fluids can migrate preferentially.

1.3 Significance and Motivation

Variations of subsurface permeability can result in an increased or decreased potential for fluid flow. In this study we analyze faults and fractures in the Cedar Mesa Sandstone - a reservoir analog type rock. These faults and fractures have in the past acted as fluid migration pathways (Petrie et al., 2013). From field observations it can be inferred that the Cedar Mesa Sandstone was host to a reducing fluid that altered the color from red/orange to light tan, brown, and white. These distinct changes in the color of the rock act as a record of the fluid flow episodes that occurred in this area. Evidence for a reducing fluid phase can also be seen in the overlying Organ Rock Formation. The color change has occurred adjacent to the faults that cut through both the Cedar Mesa Sandstone and the Organ Rock Formation. Fractures in the Organ Rock Formation that are associated with these faults also exhibit evidence of reduction due to fluid migration. From this evidence we can infer that fluids have migrated along the faults, fractures, and

associated damage zones within the Cedar Mesa Sandstone and then escaped through the seal where these structures intersect the Organ Rock Formation.

In petroleum systems faults and fractures can significantly affect the permeability of rocks, and impact the migration pathways and the quality of petroleum reservoirs (Antonellini and Aydin, 1994; Shipton et al., 2002). The natural faults and fractures that are present in the reservoir rock can act as barriers or as conduits to oil and natural gas (Nelson, 2001). Better understanding of fluid migration in these faults, fractures, and associated damage zones in reservoirs has direct significance to the oil and gas industry. One theory is that faults and fractures can act as barriers to fluid flow (Antonellini and Aydin, 1994).

In the Hite field area these faults, fractures, and associated damage zones acted as fluid conduits (Petrie et al., 2013). The Hite area is an ideal location to study this fluid-fault interaction because outcrops are very well exposed and evidence for fluid flow can easily be seen due to the stark contrast of colors in the areas around faults and fractures. The areas where fluid interactions have taken place have reduced the sandstone and surrounding formations where the structures crosscut. These faults exhibit macroscopic features that indicate they were conduits for fluid flow and alteration after the formation of low-permeability deformation bands (Petrie et al., 2013), contrary to the conventional wisdom regarding deformation-band faults in aeolian sandstones (e. g. Antonellini and Aydin, 1994; Fossen et al., 2007; Skurtveit et al., 2015).

The demand for energy usage increases the demand for oil and natural gas production (Figure 3). To meet increased demands it is important to understand fluid

migration in faulted and fractured reservoirs. Detailed outcrop characterization of

reservoir analogs provides critical information for developing accurate predictive models

of the migration of fluids in the subsurface.
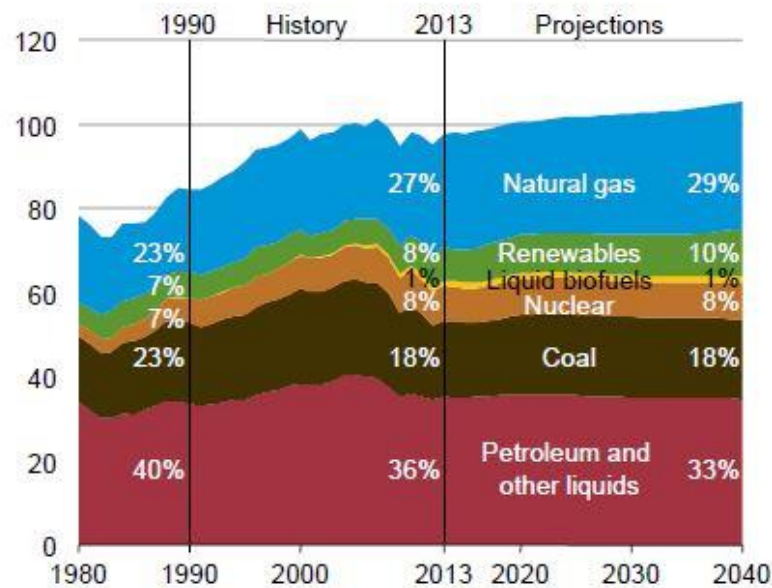
Figure 3. Primary energy consumption from 1980 to 2040. Better understanding fluid migration in certain reservoirs may play a large role in future oil and natural gas production (EIA, 2015).

1.4 Study Area Geologic Setting

The study area is located near Hite, Utah (Figure 2). The Hite Fault Group strikes

to the northwest with a large portion of the faults falling within the Glen Canyon National

Recreation Area. The primary area in this study is located just outside of the recreation

area to the south on BLM land. The fault swam is accessible due to the decline in the

water level of Lake Powell, where since 2005 the rocks in the area of the confluence of

the Dirty Devil and Colorado Rivers are exposed. The area affords map and cross sectional views of numerous faults with displacements between centimeters to ~ 10 m.

1.4.1 Depositional History

The four formations in the Hite field site that are of interest in this study include the Permian Cedar Mesa Sandstone, Organ Rock Formation, White Rim Sandstone, and the Triassic Moenkopi Formation (specifically the Upper Member of the Moenkopi Formation) (Figures 3 and 4). The key faulted outcrops examined consist of Cedar Mesa Sandstone that in some areas are capped by the overlying Organ Rock Formation (Figure 4). Geologic descriptions for each unit follow:

Cedar Mesa Sandstone: The Permian Cedar Mesa Sandstone (Pcm) is one of the four members of the Cutler Group. The Cedar Mesa Sandstone is an erg or dune field type deposit that covered a large area of southeastern Utah during the lower Permian. This arid erg environment received its supply of sediment from a marine shelf that was located to the northwest. From this shelf, sand was blown inland to the dune field (Stanesco and Campbell, 1989). Other sediments found in the Cedar Mesa Sandstone were derived from fluvial systems stemming from the Uncompahgre uplift to the northeast. In addition to this the Cedar Mesa Sandstone was also bordered by a coastal sabkha to the south (Huntoon et al., 2003).

The Cedar Mesa Sandstone consists of three lithofacies (Langford and Chan, 1988), not all of which are seen in the Hite field area. These lithofacies include the upper

most white sandstone facies, the middle red mudstone facies, and the lowest of the three, the gypsum and limestone facies. In the Hite site area we observe the white sandstone facies. This facies is dominated by quartz-rich grains that range in size from very fine to very coarse sub rounded to well-rounded grains (Huntoon et al., 2003). Cross bedding within the Cedar Mesa Sandstone can also be seen in various locations in the Hite field site.

Organ Rock Formation: The Permian Organ Rock Formation is a red to brown horizontally bedded and cross bedded formation that alternates between siltstone and medium grained sandstone (Willis, 2012). It lies above the Cedar Mesa Sandstone and is a cliff-forming unit with many friable layers. The Organ Rock Formation was deposited in a continental fluvial floodplain type environment and aeolian environment (Huntoon et al., 2003). The lower portions of the Organ Rock Formation were deposited from streams that flowed from the Uncompahgre Uplift to the north and east and from the Monument Upwarp from the south (Huntoon et al., 2003). The Organ Rock Formation is a very distinct uniform pink marker bed throughout the Hite field site and is useful for the identification of faults and fault throw.

White Rim Sandstone: The Permian White Rim Sandstone is a pale gray to yellow fine-grained silty sandstone. The depositional environment for the White Rim Sandstone was aeolian with some possible marine influence (Willis, 2012). In the Hite field site I use the White Rim Sandstone as a marker bed to identify faults since it is quite easily identified throughout the area. The White Rim Sandstone is seen as a cliff-forming

unit above the Organ Rock Formation. It is outlined in Figure 4 below. The thickness of

the White Rim Sandstone ranges from 4 - 26 meters in the Hite area (Willis, 2012).

Moenkopi Formation (Upper Member): The Upper member of the Moenkopi

Formation is the only Triassic formation present in the Hite field site, and is also the only

unit that is not part of the Cutler Group. This formation makes up the tops of the mesas in

the field site. The Upper member of the Moenkopi Formation is reddish brown and

consists of slope forming siltstones and sandstones (Willis, 2012). There are a few cliff-

forming layers within the Upper member of the Moenkopi present in the Hite field site.
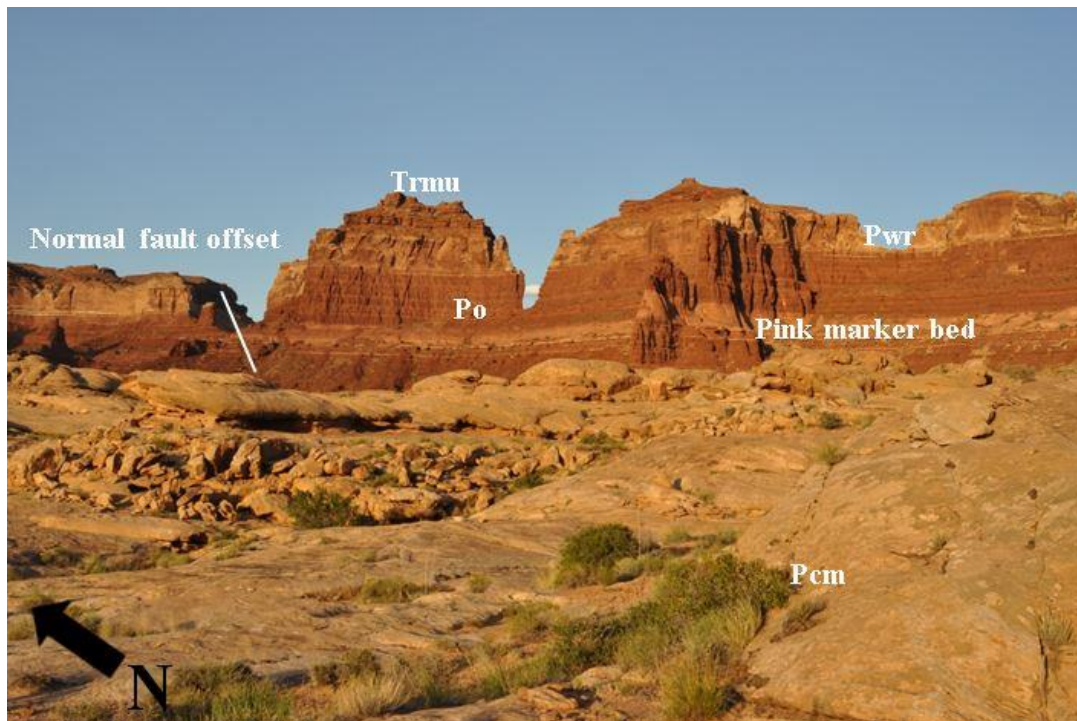
Figure 4. Stratigraphy of the Hite Field area. Trmu (Upper Member of the Moenkopi Formation), Pwr (White Rim Sandstone), Po (Organ Rock Formation), Pcm (Cedar Mesa Sandstone), and also the prominent pink marker bed within the Organ Rock Formation are clearly seen in the cliff faces.
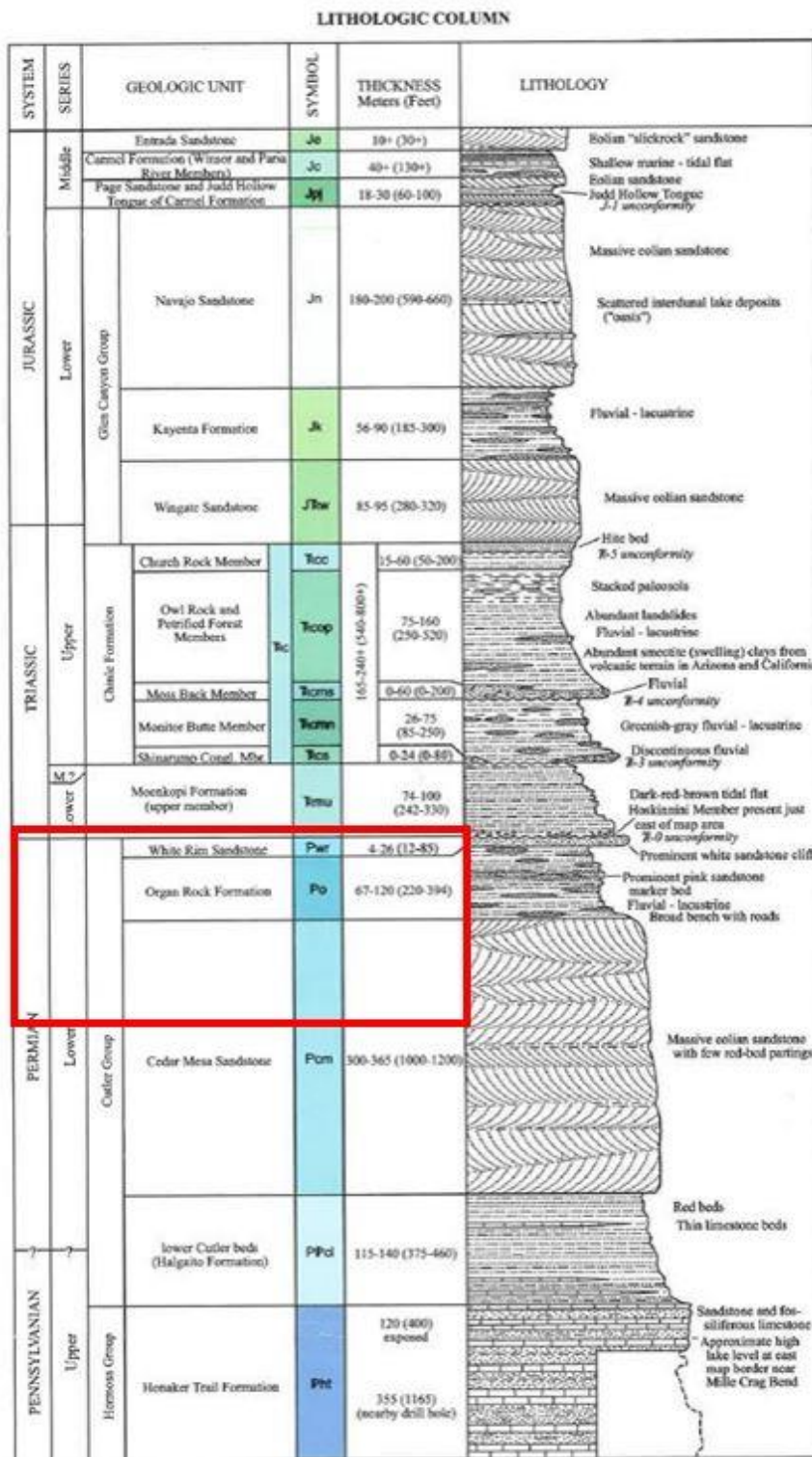
Figure 5. Stratigraphic column for the Hite field area (Willis, 2012). Outlined in red is the strata the can be observed in the Hite field area and which has been identified in Figure 4.

1.4.2 Tectonic History

Four major tectonic events affected deposition during the late Paleozoic and late Mesozoic. In southeastern Utah most of these events took place or began taking place during the Pennsylvanian, but all had some effect on sediment transport in southeastern Utah during the Permian. These four tectonic events were the Uncompahgre uplift, formation and subsidence of the Paradox Basin, the Monument Upwarp, and Laramide tectonics.

Uncompahgre uplift: The Uncompahgre uplift is a basement uplift that formed during the Pennsylvanian as part of the ancestral Rocky Mountains (Baars and Stevenson, 1981). At the same time a micro continent was colliding into the southern portion of North America (Harry and Mickus, 1998). It is proposed that stress from the collision along with the uplift of the ancestral Rocky Mountains may have made possible the basin and fault bounded uplifts that we see present in the south central part of the United States (Kluth and Coney, 1981). This resulted in the formation of the Uncompaghre highlands, which occupied a NNW trending region that is now defined by the Utah-Colorado boundary. The Uncompaghre was a source of clastic sediments during late Pennsylvanian to Permian across a wide portion of Utah and Colorado.

Paradox Basin Formation: As a result of the Uncompahgre uplift the Paradox Basin began to form. The southwestern flank of the Uncompahgre uplift is bounded by a high-angle reverse fault (Frahme and Vaughn, 1983). This reverse fault is what gave way for the development of the asymmetric Paradox Basin that subsided on the southwestern flanks of the Uncompahgre uplift (Barbeau, 2003) during the Pennsylvanian and

Permian. This allowed the basin to develop into a major depositional center (Barbeau, 2003). After this time the Cedar Mesa Sandstone was deposited. A large abundance of evaporate deposits were also deposited in the Paradox Basin in the Pennsylvanian. The movement of these evaporites has created many unique structures within the Paradox basin such as the salt-cored anticlines near Moab. The Hite field area is located approximately 15 kilometers from the zero thickness of the Paradox Basin salts.

Monument Upwarp: Some sedimentary rocks in southeastern Utah have a slight northwest dip of approximately 2°. This can be contributed to the Monument Upwarp (Goldstrand, 1994; Condon, 1997; Walsh and Schultz-Ela, 2003). The Monument Upwarp is a low topographic high in the south end of the Paradox Basin (Blakey, 1996). This large-scale tectonic event influenced the regional tectonics of southeastern Utah where the Hite field area is located.

Laramide Tectonics:

Additional major expressions of Laramide tectonics include large regional structures that include monocline formations in the San Rafael Swell, the Waterpocket Fold, and the East Kaibab monocline (Davis, 1999). There are also multiple doubly plunging anticlinal uplifts and various other smaller synclines, anticline, and monoclines associated with Laramide tectonics throughout Southern Utah (Kelly and Clinton, 1960). One of the major Laramide expressions the Waterpocket Fold is located just to the West about 50 km. There is a high possibility that Laramide tectonics had influence in the formation of the Hite Fault Group.
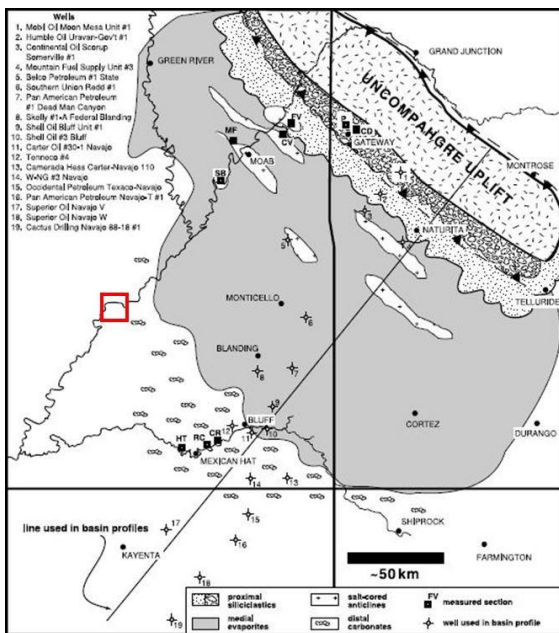
Figure 6. Paradox Basin evaporites extent map. The grey color shows the extent of the evaporites that filled the Paradox basin. Movement of these evaporites is one possible explanation for the presence of the Hite Fault Group. The approximate location of the Hite study area is outlined by the red box which is also seen in Figure 10. Modified from Barbeau, 2003.
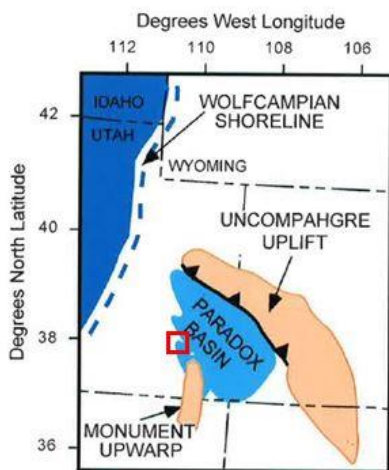
Figure 7 Uncompahgre uplift, Paradox Basin, and Monument Upwarp map. The approximate location of the Hite study area is outlined by red box. Modified from Blakey, 1996.

CHAPTER II

METHODS

A variety of field and laboratory methods were used in this project to accomplish

the study objectives. Field data collection focused on the mesoscopic-scale

characterization structures of the faults and fractures seen in outcrops of the Cedar Mesa

Sandstone. GPS recordings were taken at each outcrop where orientations were gathered.

These locations were outcrops containing faults, associated damage zones, or fractures

sets. NAIP imagery of the field area with 1 meter resolution was compiled and rendered

using false colors to make faults more easily identifiable prior to mapping them in the

field. An example of this false color image is included in the appendices (Figure 12).

Mapping of faults and associated damage zones was done on 1:10,000 scale maps that

were created in ESRI Arc GIS 10.3.1. Field notes for each site include descriptions of the

host rock, names of the locations, widths of the damage zones, types of mineralization

and alteration along fractures, photographs of the outcrops and damage zones, and any

other unique descriptive characteristics of the outcrop. These data have been compiled in

Arc GIS software, using the mapped fault orientations and width of the damage zones.

Proximity of each fault was determined by measuring map distances between the fault

surfaces The Arc GIS maps show the locations and orientations of the faults and damage

zones. From these data, I measured the distance between each location to have some

sense of proximity between the fault locations. Using this proximity data we try to

correlate geochemical data between the locations. The data that was collected can be used

in the future to populate a 3D model that will act as a fluid flow simulation model for the fractured and faulted Cedar Mesa Sandstone reservoir.

Representative fault damage zones width and internal structure were characterized by measuring the fracture distribution within each zone. Three faults were selected from the group surveyed and at each of these more detailed data was needed. To collect data, linear scan lines were used to systematically characterize the fault and associated damage zone. All scan lines were setup where the zero would be in protolith sandstone of the hanging wall. Data and samples were collected at intervals chosen in the field for each specific linear scan line. These intervals were chosen to intersect the fault surface and to prevent bias in other zones of the scan line. When it was possible oriented samples were collected at each location. The samples collected were used in petrology and geochemical analyses.

Three faults with a range of throws and associated damage zone widths that give the best representation of the faults surveyed within the Hite field area were selected to be analyzed in greater detail. To have a good representation of the fault group I chose faults with the smallest, moderate, and largest throw. The faults were named in the same order that analysis was performed in the field. Fault locations and amount of throw on each fault can be seen in Table 1 below.

Table 1. A list of the major study faults and their locations.

Faults	Throw (m)	Location (UTM, zone 12N)	
F1	7	4188283.39	559549.24
F2	0.25	4187697.90	559854.19
F3	2	4188004.72	558346.33

Sample collection was done along linear scan lines that were oriented perpendicular to each fault outcrop. At the F1 outcrop a 57-meter long scan line was set up perpendicular to the northwest (305°) striking fault. The edge of the scan line was marked as zero at selected at a distance from the fault surface and fault damage zone where we believed that protolith Cedar Mesa Sandstone unaltered by fault existed. In other faults with smaller damage zones the scan lines were shorter to avoid collecting excess data in protolith Cedar Mesa Sandstone. The protolith was defined in the field as an area with a low fracture density that was believed to be similar to unfaulted and damaged Cedar Mesa Sandstone. At outcrop F1 19 samples were collected every 3 meters. Samples collected were oriented and were large enough so that multiple thin sections could be made and enough material could be set aside for XRD and XRF analysis. Fracture densities were recorded along the entire scan line and were averaged over three meter intervals. Fracture densities were plotted for F1, F2, and F3 on rose diagrams using OpenStereo. Field permeability measurements were also collected every 3 meters using a TinyPerm II. All permeability measurements were taken directly at the interval along the line where it fell on a fracture or between fractures in unfractured host rock.

Sample and data collection techniques for outcrops F2 and F3 were similar to methods used for F1. The differences were the length of the scan line and the interval at which data were collected at outcrops F2 and F3 a portable handheld core drill was used to collect samples of approximately 4 to 5 inches in length with a 1 inch diameter.

The scan line set up for Fault F2 was about one third the size of the one set up for Fault F1. With this in mind fracture density and measurements were taken along the entirety of the line while samples and permeability measurements were collected every meter instead of every 3 meters along the 15-meter long linear scan line which was set up here. Approaching the fault surface, samples and permeability measurements were collected every 0.5 meters. The handheld core drill that was used to collect samples for sites F2 and F3 can be seen in Figure 29A.

For Fault F3 the linear scan line was a slightly over one half the size of the one sent for Fault F1. With this in mind the fracture density and measurements were taken along the entirety of the line while samples and permeability measurements were collected every 1.5 meters instead of every 3 meters along the 36-meter long linear scan line which was set up here.

A portable ultraviolet light was used to observe fluorescent minerals found within the damage zones (Petrie et al., 2013). Many of the fractures in the damage zones are mineralized with calcite that fluoresces when present in trace amounts (MacRae and Wilson, 2008). The UV illumination allows us to examine fluorescent fractures and determine the presence of subtle mineralization and crosscutting relationships not typically seen in daylight conditions. If some calcite filled fractures exhibit different

colors of fluorescence we estimate what trace element or mineral is causing the color change (MacRae and Wilson, 2008). From this we imply what chemical changes could have taken place to cause these differences in fluorescence.

Laboratory analyses included optical petrography, X-Ray diffraction (XRD), and X-Ray Fluorescence (XRF). Optical petrography allows us to examine microscopic-scale structures and features such as deformation bands and fractures. Mineral identification and fractured grain analysis were done for each thin section. Point counts of 200 grains were done on three slides from each outcrop to determine feldspar content of the Cedar Mesa Sandstone in the study area. Crosscutting relationships and deformation textures were identified. Digital photomicrographs were taken of all prepared thin sections to be used to define small-scale structures. A total of 94 thin sections were evaluated analyzed from faults F1, F2, F3, and surrounding fractures. By combing results from thin section petrography, whole-rock mineralogy analysis using X-Ray diffraction (XRD), and whole rock chemical analysis (XRF) of each sample we were able to characterize mineralogy of the host rock, mineralogy of the fractures, lithology, sedimentary patterns, textures, and fracture characteristics. This lets us evaluate mineralogy between protolith Cedar Mesa Sandstone and faulted or damaged sandstone.

X-ray diffraction analyses were completed at the USU Geology XRD Lab using a Philips PANalytical X'Pert X-Ray Diffractometer (XRD). Each scan was run using CuKα radiation at 45kV and 40mA and from 0° to 75° 2Θ. The software PANalytical X'Pert Data HighScore, version 2.2.0 was used to analyze and interpret the mineral peaks from the XRD spectra. A total of 18 samples were processed. XRD analysis was

performed on 6 samples from each outcrop which consisted of two protolith samples, two

samples from the center of the damage zone, and two samples from areas of question

related to the damage zones.

Whole-rock x-ray fluorescence (XRF) analyses were performed by SGS

laboratories in Canada. The lab performed a borate fusion in preparation for the XRF

whole rock analysis to examine for 14 major and minor elements. A total of 19 samples

were processed from outcrop F1. The samples from the other study sites were

contaminated by drill core cutting oil.

CHAPTER III

RESULTS

Most of the exposures examined in this study (Figure 12) consist of normal faulted Cedar Mesa Sandstone, Organ Rock Formation and Upper Red Member of the Moenkopi Formation. The Cedar Mesa Sandstone is a fine-grained, well sorted, and well-cemented, cross-bedded sandstone. The buff tan to brown color of the Cedar Mesa Sandstone is uniform throughout the area. This color is possibly due to the chemical alteration of this sandstone by a reducing fluid that was once present (Chan et al., 2000). Orientations of the 34 normal faults the are similar, striking from 294° and 315° and dipping from 73° to 85° (Table 2; Figure 9). The traces of the faults in the area are continuous for 100's of meters up to multiple kilometers (Figure 1; Figure 11; Figure 10). Maximum displacements of the faults surveyed in this area range from 0.25 meters to 7 meters, based on offset in marker beds.

N = 34
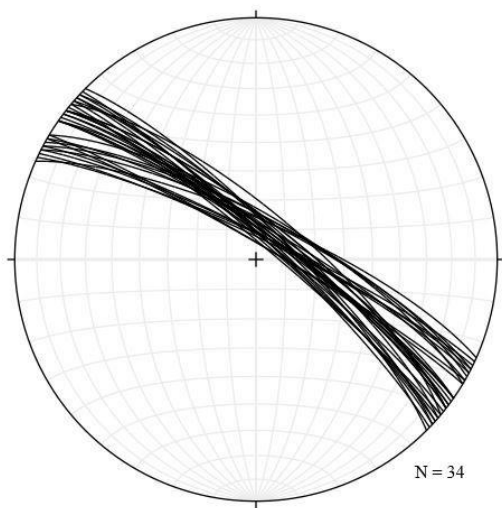
Figure 8. Stereonet of all faults surveyed in the Hite field area. The corresponding attitude data is displayed in Table 2.
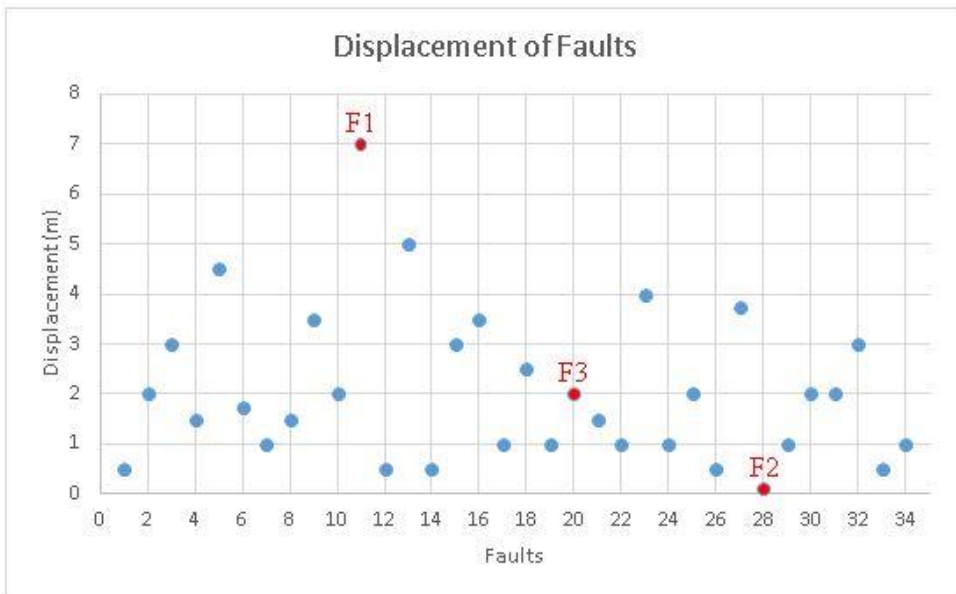
Figure 9. Maximum fault displacement measured on 34 measured faults in the Hite field area. The average displacement of these 34 faults is 2.08 meters. Red dots on this figure represent faults that were studied more in depth (F1, F2, and F3).
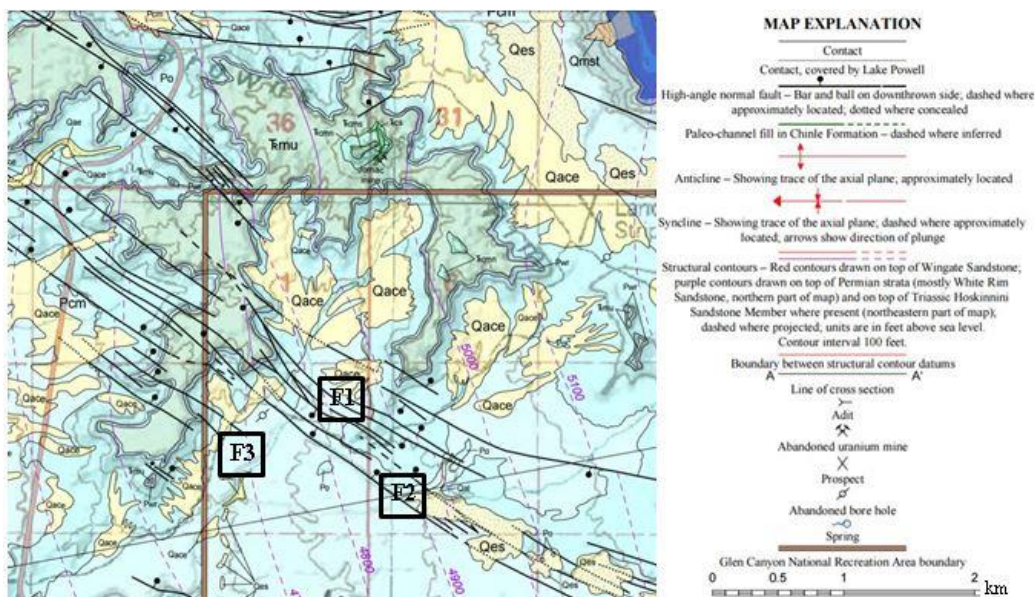
Figure 10. Geologic map showing sites F1, F2, and F3 and related geology. The Glen Canyon National Recreation Area boundaries displayed as a bold brown line. Modified from (Thaden et al., 2008).

Table 2. Orientations of all 34 surveyed faults in the Hite Field Area.

Fault	Strike (degrees)	Dip (degrees)	Displacement (m)	Study Sites
1	312	81	.5	
2	308	80	2	
3	298	76	3	
4	296	83	1.5	
5	301	85	4.5	
6	297	77	1.75	
7	313	79	1	
8	305	82	1.5	
9	308	77	3.5	
10	307	81	2	
11	305	79	7	Site F1
12	299	76	.5	
13	300	85	5	
14	305	81	.5	
15	314	83	3	
16	311	78	3.5	
17	295	82	1	
18	294	77	2.5	
19	315	79	1	
20	308	80	2	Site F3
21	313	82	1.5	
22	298	82	1	
23	301	75	4	
24	311	84	1	
25	312	83	2	
26	308	77	.5	
27	297	82	3.75	
28	306	81	.25	Site F2
29	310	85	1	
30	307	80	2	
31	309	83	2	
32	305	81	3	
33	310	74	.5	
34	300	79	1	
Average	**305.24**	**80.26**	**2.08**	
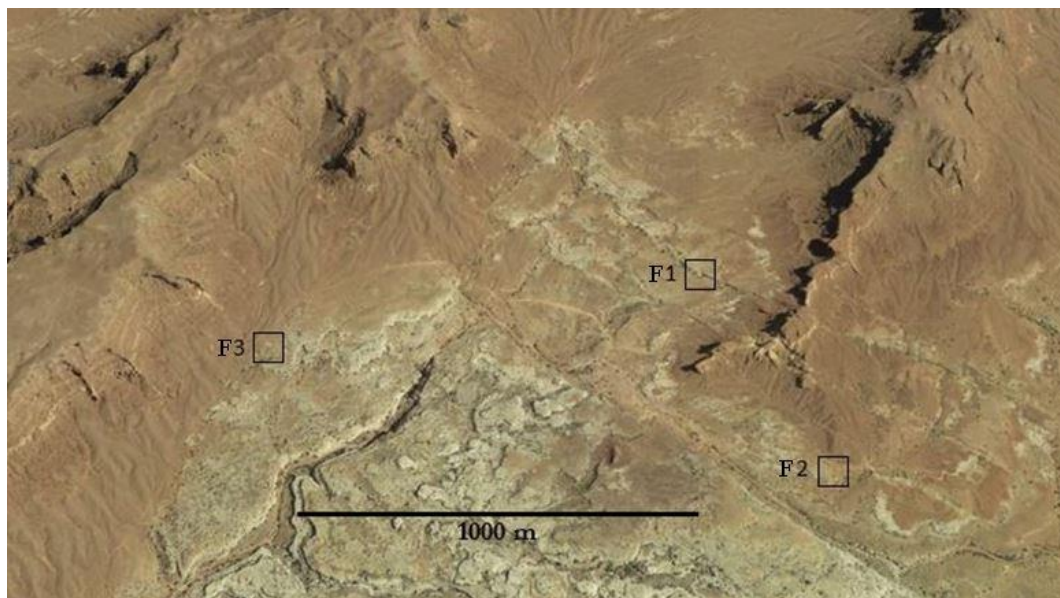
Figure 11. Google Earth image of site locations F1, F2, and F3.

Figure 12. False color NAIP imagery that was used to identify possible faults before field work.

3.1 Fault F1
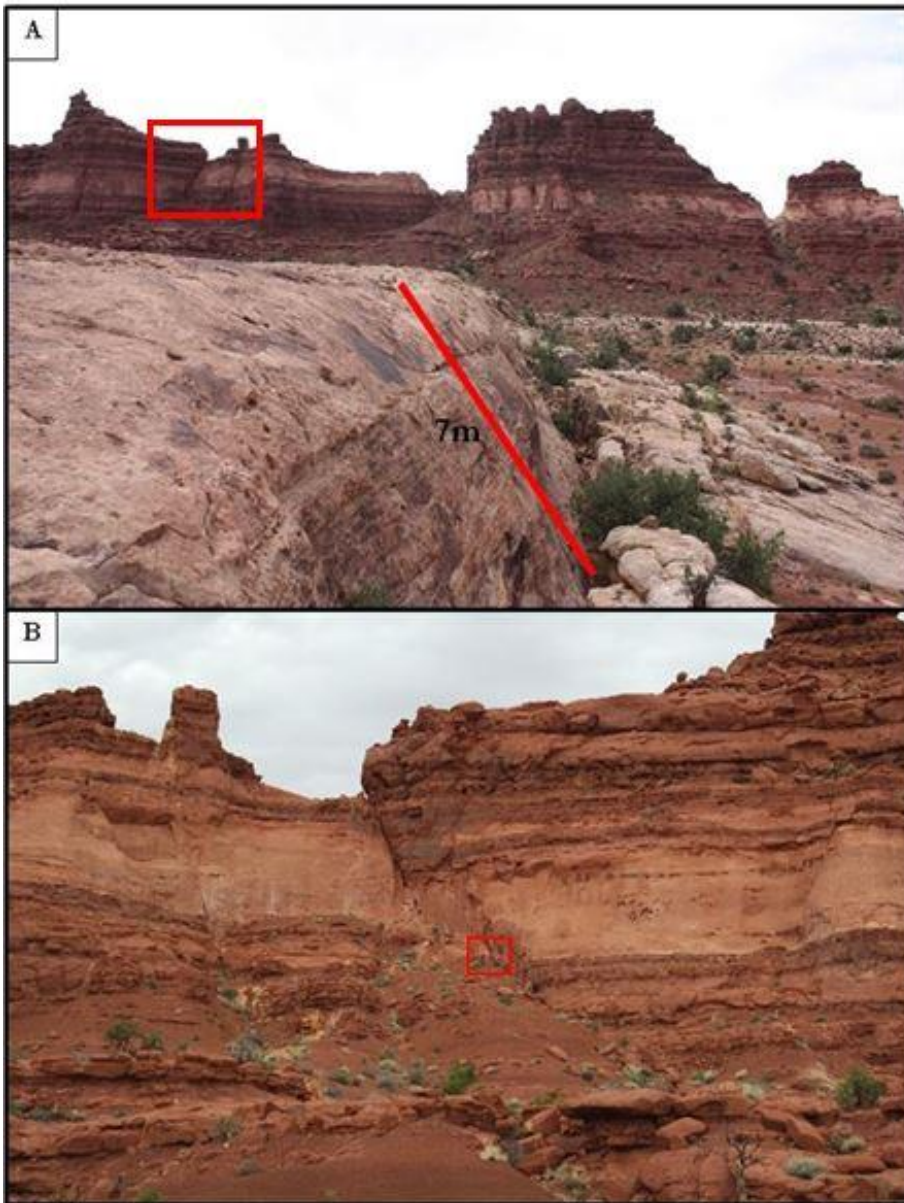
Figure 13. View of site F1, with view of the largest throw in the study area. Image A shows the size and orientation of the fault studied at site F1. In image A the view is at roughly 125° azimuth. The red line in image A shows the fault plane and the throw of the fault which is 7 meters. The red box in image B surrounds me at a height of 5 feet 10 inches for scare next to the pink sandstone member. The fault in image B is not Fault F1 but rather a location on the other side of the ridge looking in about a 305° azimuth. This is where I could get close to the pink sandstone member safely for scale. The fault in image B can be seen in the cliff face to the upper left of image a highlighted by a red box.
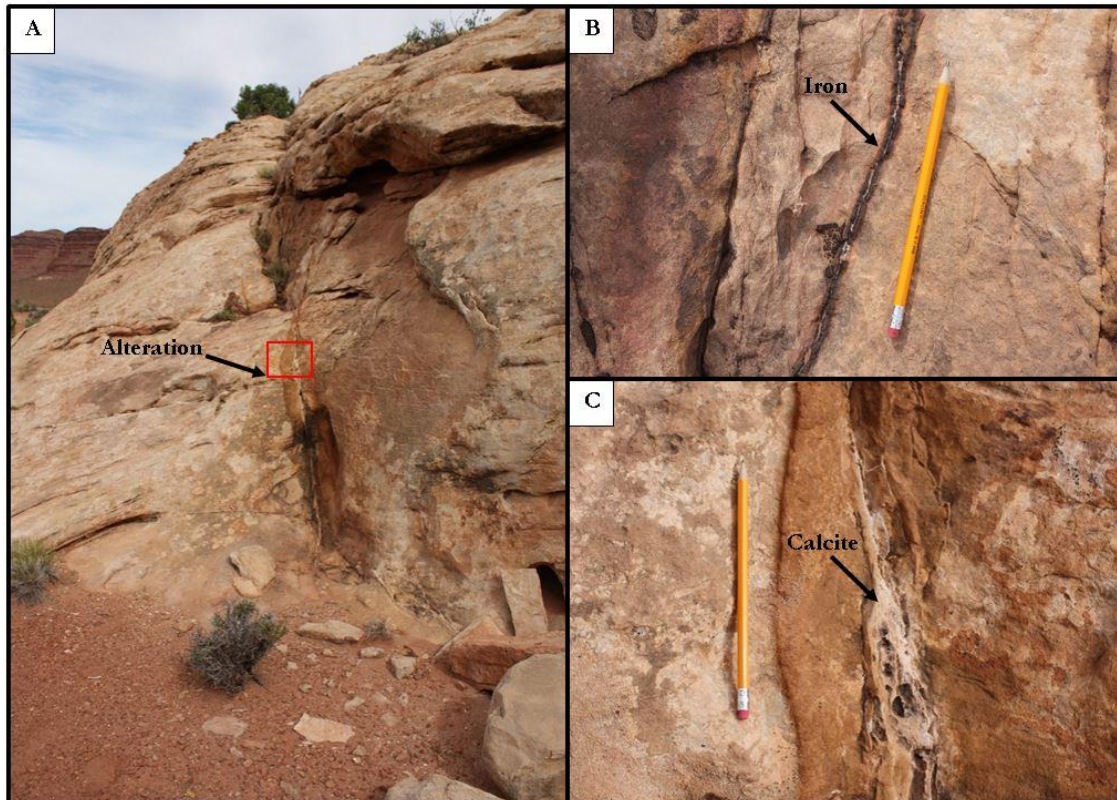
Figure 14. Fault F1 photo overview of fractures, alteration, and types of mineralization. Site F1 is the fault with the largest throw in the study area. Images A through C all show various areas of site F1. Images A, B, and C show the fault surface and examples of fractures related to the damage zone surrounding Fault F1. Image C is a closer view of the red box outlined in image A that surrounds and pencil for scale. Alteration and mineralization of the fractures can be more easily viewed in image C.

We examined three faults and associated damage zones to test the hypothesis that fluids can migrate preferentially along small displacement faults in sandstones. These three faults were chosen from a group of 34 measured faults (Table 2; Figures 7 – 10) that represent end members of fault throw. Whole-rock XRF analyses were performed on 19 samples from site F1. The XRD analyses were performed on selected samples from each site. Thin sections were examined from all samples collected at sites F1, F2, and F3.

The locations of these sites are shown in Figures 8 and 9. Initially the width of the bleached zone versus the throw of the fault was being used to characterize each fault. After surveying many faults in the area a correlation between fault throw and width of the bleached zone was not seen.

At site F1 a 57-meter long scan line was set up for data and sample collection (Figure 15). This scan line starts outside the damage zone to the southwest of the fault, runs perpendicular across the Fault F1 which is trending at 305°, and extends past the edge of the damage zone to the northeast for approximately 25 m. A total of 80 fracture sets was measured along this scan line. All data mentioned in the methods section for Fault F1 was collected on the line shown in Figure 15 below.

Figure 15. Scan line location at site F1. View to the Northeast from meter 0.

3.1.1 Fault F1 Orientation and Fracture Analysis

Fault F1 has the greatest throw in the study area, 7 meters at its maximum, and it strikes 305°, dips 79° SW (Figure 9). The fault geometry data for F1 was collected along the scan line shown above in Figure 15. The scan line across Fault F1 traverses the fault at a location where the outcrop was well exposed and data could be easily collected (Figure 15 and Table 1). One of the other locations is approximately 500 meter southeast of the scan line and the other about 1 kilometer to the northwest of the scan line (Figure 11). To the northwest Fault F1 strikes at 305° and dips at 80° SW and to the southeast Fault F1 strikes at 303° and dips at 79° SW. At both other locations the offset of the fault is also 7 meters. The offset of the fault was measured using a prominent 7m thick stratigraphic member of the overlying Organ Rock Formation, where the prominent 7m-thick pink member is offset.

In outcrop, fractures are observed with increasing frequency from SW to NE as we transitioned from the protolith sandstone in the sandstone into the damage zone (Figure 17). As the fault surface is approached the fractures increase and then a sharp decrease is seen at the core of the fault and at the fault surface (Figure 17). Iron oxide alteration of the sandstone can be seen along the fault surface and near the present fractures. Iron mineralization can be seen along the outer edges of the fracture with calcite mineralization in the center of the fracture (Figure 14), but not all fractures are mineralized with both iron and calcite. In areas the fault surface is mineralized with iron. The most visible iron oxide alteration in the sandstone is observed around the fractures.

In outcrop the damage zone is identified by increased fracture density adjacent to the fault surface, and damage zone width is 19 to 21 meters wide at 3 locations. The damage zone is also recognized by a change in color of the sandstone where brown, orange, and red tones from the greater amount of iron oxide alteration took place. The majority of fractures present in this outcrop exhibit similar strikes and dips to Fault F1. The strikes the measured fractures can be seen in Figure 16 where the average strike is shown as 302.5^o. The average dip for this set of fractures is 80.36^o.

F1 Fractures

panel

n = 80

max = 58.75 %

(frequency)

Mean dir.: 302.5°

95 % conf.: ± 0.9°

N

60 %

60 %
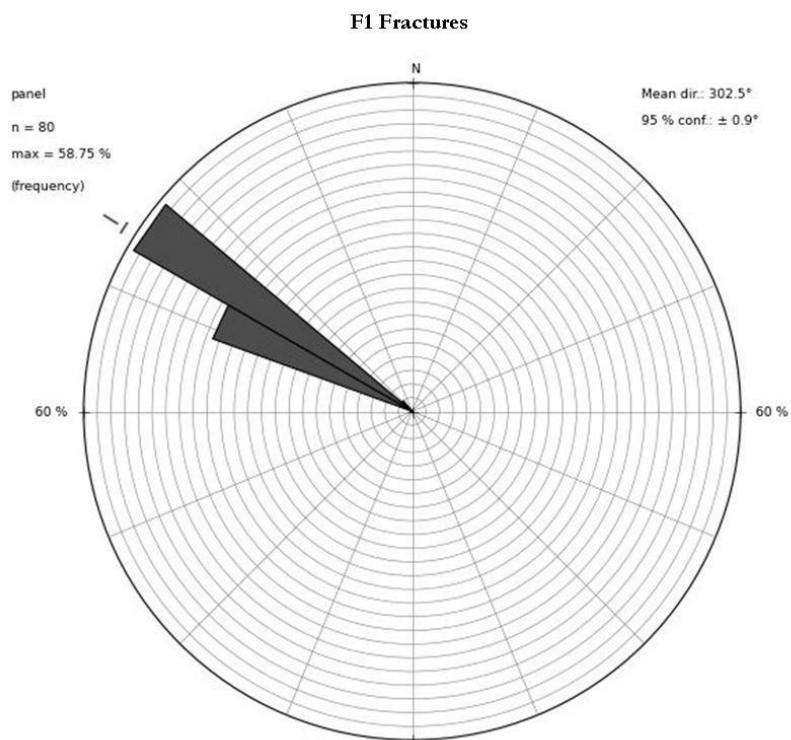
Figure 16. Rose diagram of F1 fractures. 80 fracture orientations collected at site F1 created with OpenStereo.
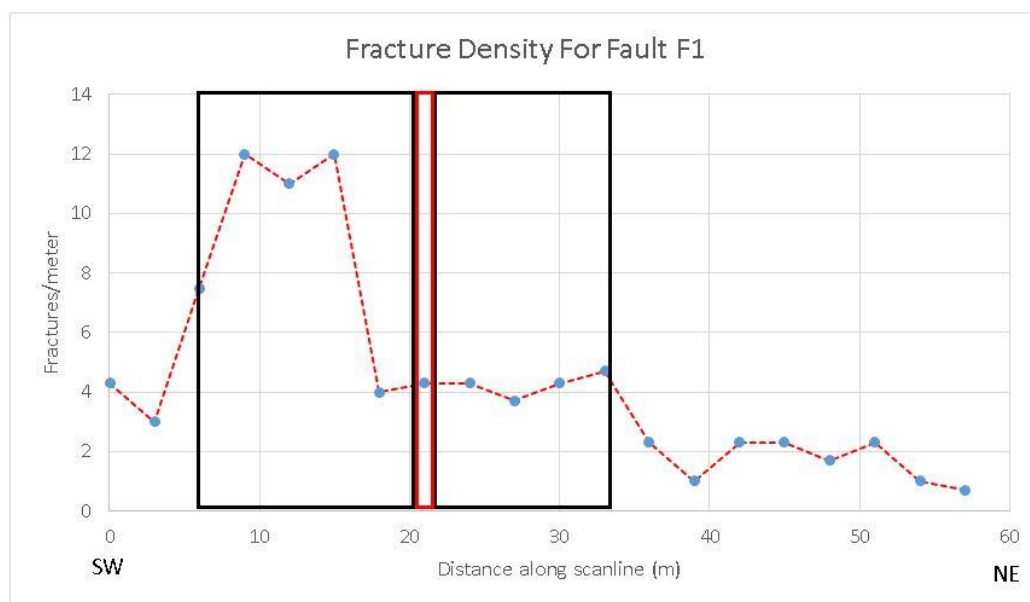
Figure 17. Fracture density collected across Fault F1. Fracture density is displayed in number of fractures per meter. The fault surface occurs at meter 21 of the scan line. The red box outlines the fault surface/core and the black boxes outline the damage zone on either side.

The damage zone surrounding Fault F1 is ~27 meters wide, and is defined by the increased fracture density from number of fractures per meter at 6m up to the fault surface at 21m and then from 21m to 33m (Figure 17). At 57 meters the fracture density drops to about 1 fracture/m which is interpreted as protolith. From the initial survey of other faults in the area, fracture density in the Cedar Mesa Sandstone protolith also was about 1 fracture/m.

3.1.2 F1 Permeability

In situ permeability measurements indicate that permeability increases within the damage zone to the southwest of the fault surface at 6 meters to 21 meters and then drops at the fault surface before increasing in the damage zone to the northeast of the fault up to

meter 33. The data collected shows these increases and decreases in permeability across

Fault F1 (Figure 18). Outside the damage zone the permeability increases and decrease

most likely due to the fracture density at that location.

Figure 18. F1 permeability chart. Permeability across Fault F1 determined with the
TinyPerm II instrument. The locations of the fault surface and damage zones are outlined
in red and black boxes as in Figure 17. The spike at meter 57 is likely due to a poor
quality measurement taken in the field with the TinyPerm tool.

3.1.3 F1 Whole Rock Geochemistry

The X-Ray Fluorescence whole-rock geochemical analysis was performed on 19 samples from Fault F1. Data for major and minor elements were reviewed for each sample. These data are displayed below in Table 3.
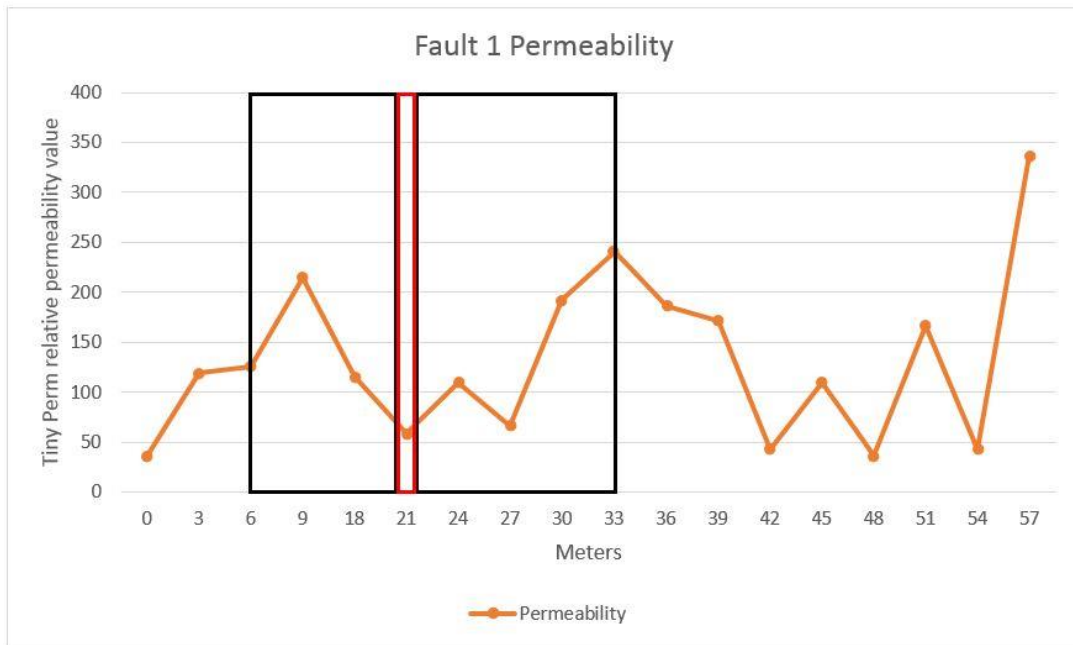
Table 3. Major and minor oxide data from XRF analyses of all samples collected along the 57 meter scan line set up across Fault F1. All data are displayed in weight percent.

Sample	SiO_2	Al_2O_3	Fe_2O_3	MgO	CaO	K_2O	Na_2O	TiO_2	MnO	P_2O_5
a-00	95.7	2.49	0.26	0.11	0.17	1.45	0.05	0.07	0	0.02
a-3	95.7	1.49	0.12	0.09	1.47	0.95	0.04	0.03	0	0.01
a-9	95.6	1.3	0.12	0.11	1.59	0.8	0.04	0.02	0	0
a-12	91.8	1.78	0.17	0.62	2.01	0.99	0.1	0.03	0	0.01
a-15	97.8	1.38	0.4	0.09	0.08	0.83	0.03	0.03	0	0.01
a-18	91.4	2.23	0.23	1.08	1.88	1.2	0	0.07	0	0.02
a-21	86.6	1.38	0.66	0.91	4.91	0.77	0.07	0.04	0	0.01
a-24	94.7	1.52	0.17	0.11	1.6	0.88	0.04	0.03	0	0
a-27	88.6	2.06	1.04	0.69	3.36	1.15	0.04	0.04	0	0
a-30	88	1.52	0.25	1.69	3.19	0.88	0.07	0.03	0	0
a-33	95.5	1.66	0.68	0.11	0.04	0.97	0.06	0.04	0	0
a-36	88.8	2.35	0.48	1.26	2.42	1.19	0.04	0.07	0	0.02
a-39	92.9	1.92	0.25	0.1	0.13	1.09	0.04	0.05	0	0
a-42	81.7	1.41	0.27	2.34	6.47	0.85	0.05	0.04	0.01	0
a-45	80.8	1.83	0.35	2.29	6.07	1.06	0.02	0.05	0.01	0.01
a-48	85.3	1.65	0.34	1.73	4.65	0.94	0.03	0.05	0.01	0
a-51	81.8	1.31	0.51	3.12	5.33	0.8	0.04	0.04	0.02	0.01
a-54	75.6	1.67	0.56	3.96	7.42	0.97	0.05	0.05	0.04	0.01
a-57	94.8	2.11	0.14	0.1	0.66	1.24	0.07	0.05	0	0.02

Figure 19. Data overview of F1 including XRF, fracture density, and permeability data. Image from Google Earth showing the location of the scan line across Fault F1 in red. Overlaying the image is a graph of major oxides in weight % /SiO_2. Below this is a graph of permeability and fracture density. Six locations along the scan line were highlighted which represent significant changes in the XRF data. These are labeled A though F above.
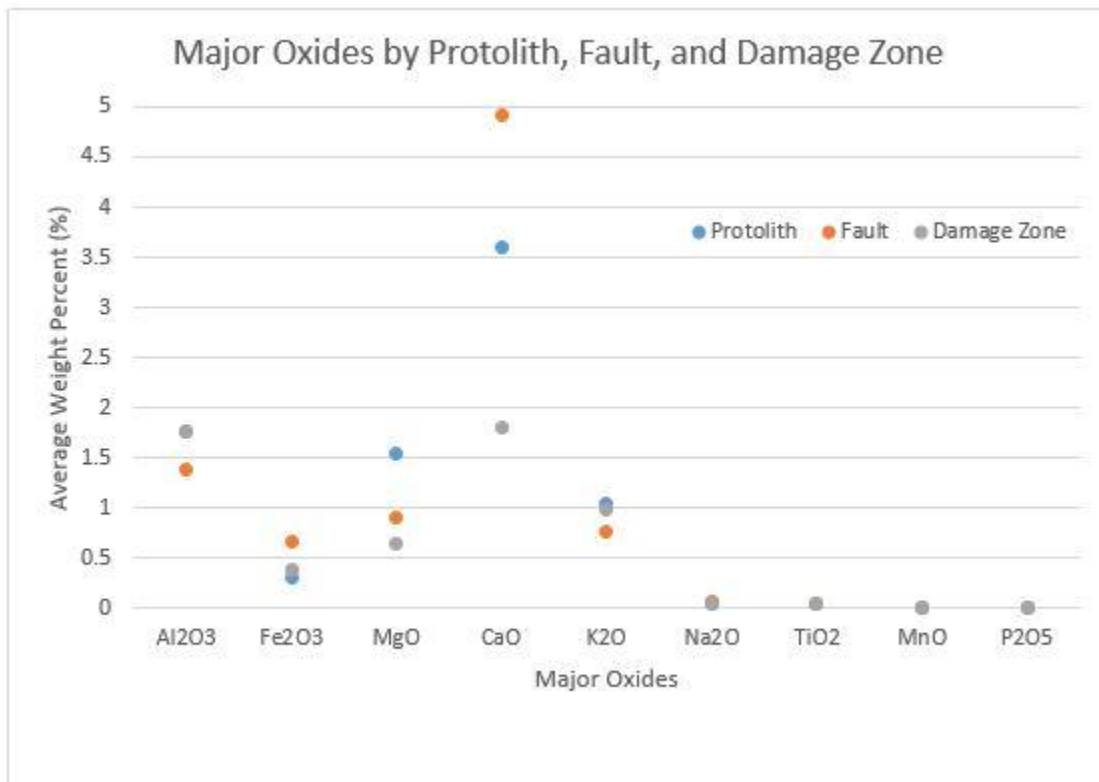
Figure 20. Major oxides by zone for Fault F1. Comparison of samples based on whole-rock chemistry, excluding SiO_2. Samples were placed into three categories, protolith, fault, and damage zone.

Major elements analyzed in the whole rock samples include Si, Al, Fe, Mg, Ca, K, Na, Ti, Mn, P, Cr, and V. Only the first six of these elements had $\geq 0.5\%$ so we only discuss these. All major oxide data mentioned below can be found in Table 3. SiO_2 is the most common major oxide of all that were analyzed accounting for 89.64% on average. The second highest weight percent is CaO with 2.81% followed by Al_2O_3 at 1.74%. At the fault the SiO_2 measures 86.6%, CaO increases above the average to 4.91%, and Al_2O_3 decreases below average 1.38%. In the damage zone SiO_2 increase to 92.47% while CaO decreases to 1.80% and Al_2O_3 stays close to the average at 1.76%. In the protolith area

the SiO_2 is slightly less at 87.14% while CaO is above average at 3.6% and Al_2O_3 stays

close to average at 1.76%. The damage zone exhibits the highest levels of SiO_2 and the

lowest levels of CaO. Al_2O_3 stays relatively consistent through all zones. The highest

level of CaO is seen at the fault and the lowest levels of SiO_2 are observed. In areas of the

fault where there is a transition from the damage zone to the fault core there are

significant variations in the major oxides.

Table 4. Major oxides separated into protolith, fault, and damage zone.

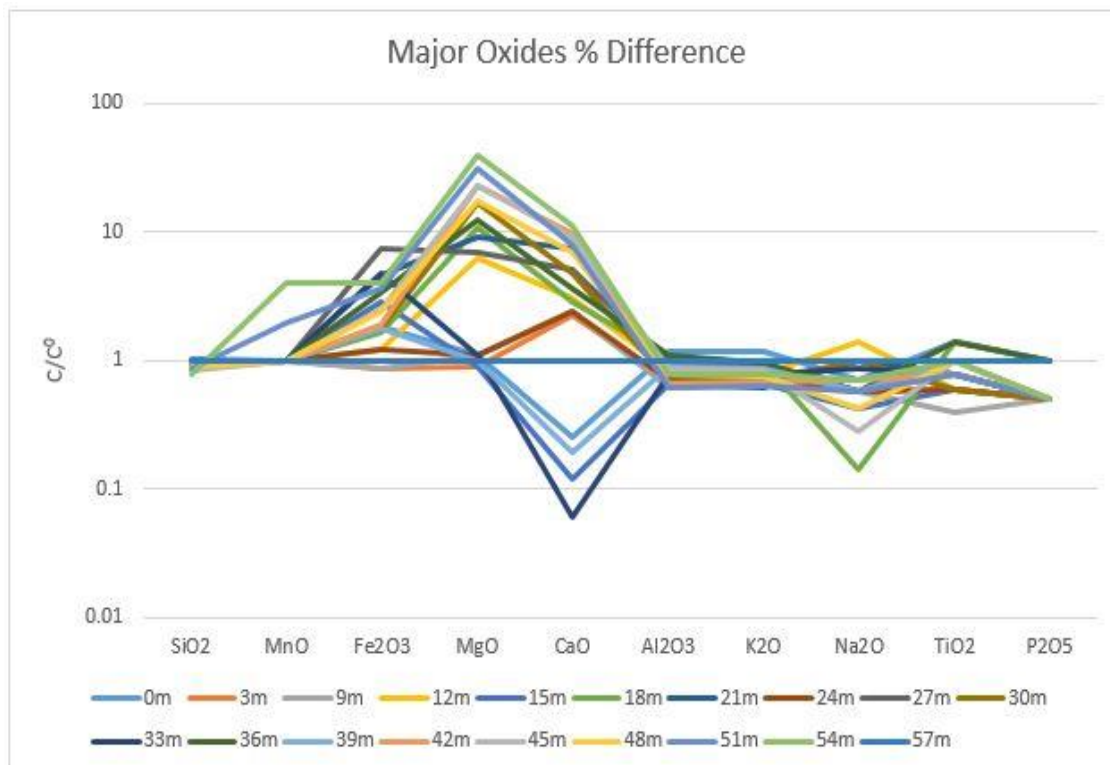| Protolith									
	SiO_2	Al_2O_3	Fe_2O_3	MgO	CaO	K_2O	Na_2O	TiO_2	MnO	P_2O_5
a-00	95.7	2.49	0.26	0.11	0.17	1.45	0.05	0.07	0	0.02
a-3	95.7	1.49	0.12	0.09	1.47	0.95	0.04	0.03	0	0.01
a-39	92.9	1.92	0.25	0.1	0.13	1.09	0.04	0.05	0	0
a-42	81.7	1.41	0.27	2.34	6.47	0.85	0.05	0.04	0.01	0
a-45	80.8	1.83	0.35	2.29	6.07	1.06	0.02	0.05	0.01	0.01
a-48	85.3	1.65	0.34	1.73	4.65	0.94	0.03	0.05	0.01	0
a-51	81.8	1.31	0.51	3.12	5.33	0.8	0.04	0.04	0.02	0.01
a-54	75.6	1.67	0.56	3.96	7.42	0.97	0.05	0.05	0.04	0.01
a-57	94.8	2.11	0.14	0.1	0.66	1.24	0.07	0.05	0	0.02
Fault									
	SiO_2	Al_2O_3	Fe_2O_3	MgO	CaO	K_2O	Na_2O	TiO_2	MnO	P_2O_5
a-21	86.6	1.38	0.66	0.91	4.91	0.77	0.07	0.04	0	0.01
Damage Zone									
	SiO_2	Al_2O_3	Fe_2O_3	MgO	CaO	K_2O	Na_2O	TiO_2	MnO	P_2O_5
a-9	95.6	1.3	0.12	0.11	1.59	0.8	0.04	0.02	0	0
a-12	91.8	1.78	0.17	0.62	2.01	0.99	0.1	0.03	0	0.01
a-15	97.8	1.38	0.4	0.09	0.08	0.83	0.03	0.03	0	0.01
a-18	91.4	2.23	0.23	1.08	1.88	1.2	0	0.07	0	0.02
a-24	94.7	1.52	0.17	0.11	1.6	0.88	0.04	0.03	0	0
a-27	88.6	2.06	1.04	0.69	3.36	1.15	0.04	0.04	0	0
a-30	88	1.52	0.25	1.69	3.19	0.88	0.07	0.03	0	0
a-33	95.5	1.66	0.68	0.11	0.04	0.97	0.06	0.04	0	0
a-36	88.8	2.35	0.48	1.26	2.42	1.19	0.04	0.07	0	0.02

Figure 21. Major oxide percent difference. Normalization of major elements from 0 to 57 meters for Fault F1. Major elements normalized to protolith sample from meter 57.

All XRF data was normalized against a protolith sample that was collected at meter 57 of the scan line. The 57 meter sample was chosen as protolith based the lack of mesoscopic alteration and fracture density at this point. Major oxide concentrations vary with structural position, and help define different zones of the outcrop. From Figures 18 and 19 it can be seen that the fault surface at meter 21 is elevated in CaO which makes it more easy to identify. Major oxides are arranged in groups with MnO and Fe_2O_3 likely derived from clays and hematite, MgO and CaO representing dolomite and calcite, Al_2O_3, K_2O, and Na_2O representing feldspars and Al_2O_3, K_2O could represent clays as well.

Figure 22. Normalization of major elements from 0 to 12 meters for Fault F1. Major elements normalized to protolith.
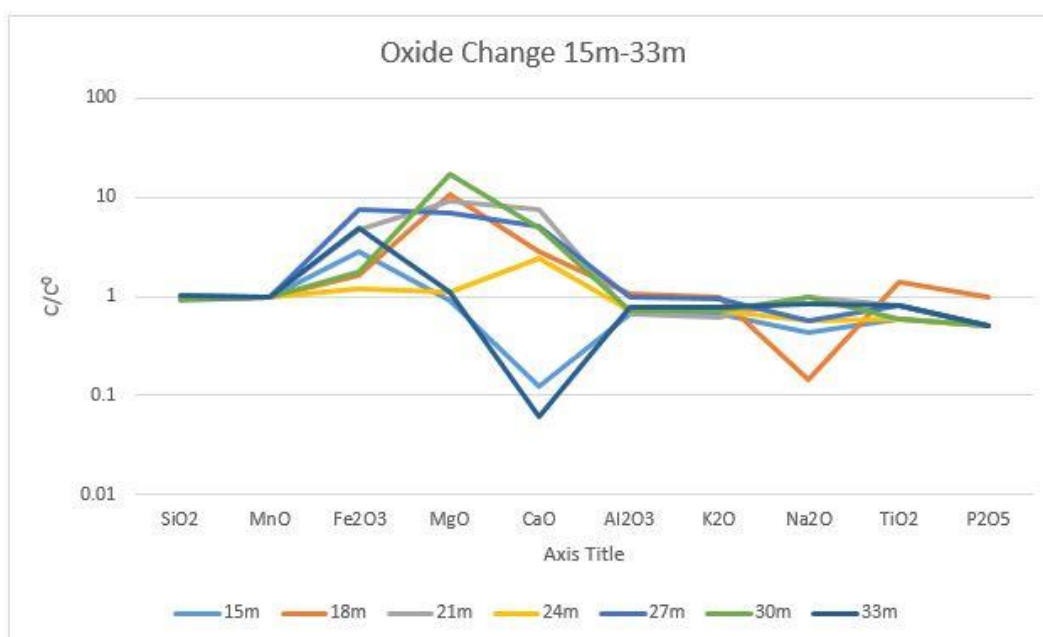

Figure 23. Normalization of major elements from 15 to 33 meters for Fault F1. Major elements normalized to protolith.
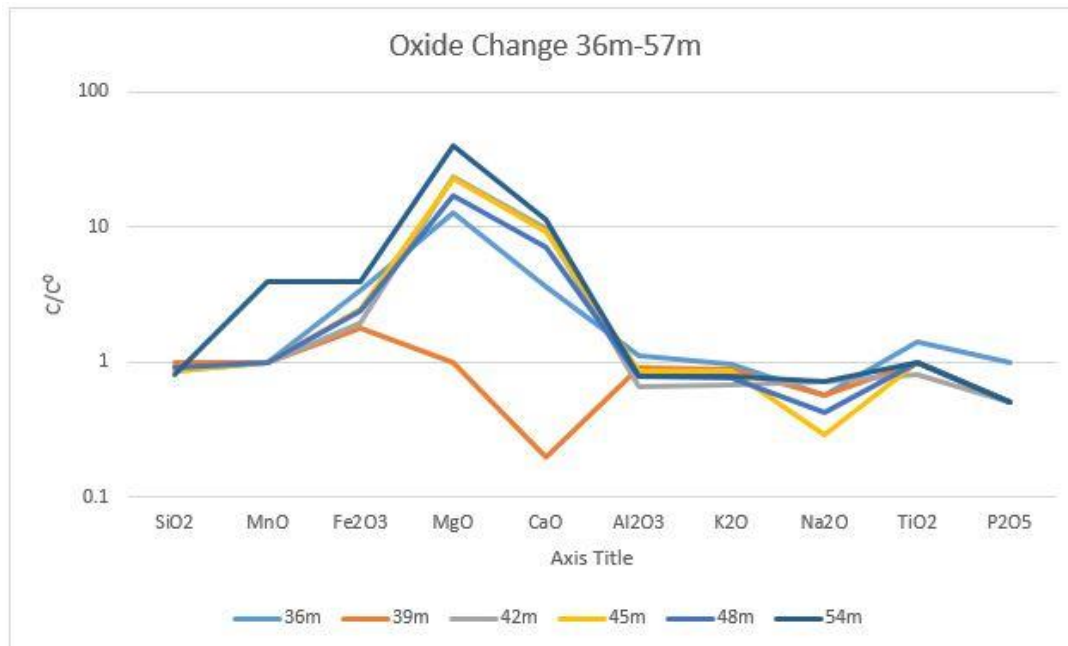
Figure 24. Normalization of major elements from 36 to 57 meters. Major elements normalized to protolith.

3.1.4 F1 X-Ray Diffraction Analysis

Seven whole-rock samples from the fault zone, damage zone, and host rock/protolith were analyzed using X-ray diffraction to determine the major rock-forming minerals. In general the samples contain different combinations of quartz and carbonates. The most common carbonate is calcite, followed by dolomite, and aragonite.

Quartz is in every sample and has the greatest intensities. Calcite is most commonly found in samples from the protolith and at the fault surface. Dolomite is also interpreted in one sample from the protolith close to the boundary of damage zone and protolith on the NE side of the fault. Aragonite is found in the damage zone on either side of the fault.

Table 5. Minerals present in the XRD analyzes at each tested location along the scan line. The fault surface is at 21 and damage zones between 6 and 21 and 21 and 33 meters.

0m	9m	15m	21m	27m	36m	57m
Quartz	Quartz	Quartz	Quartz	Quartz	Quartz	Quartz
Calcite	Calcite	Aragonite	Calcite	Aragonite	Dolomite	Calcite

Table 6. Data gathered from XRD analysis of samples in Fault F1 broken down by protolith, damage zone, and fault surface/core showing percentage of samples containing each mineral. This table shows that 100% of samples from the protolith zone of the fault contained quartz, 75% contained calcite, 0% contained aragonite, and 25% contained dolomite. Data from other zones are also displayed below.

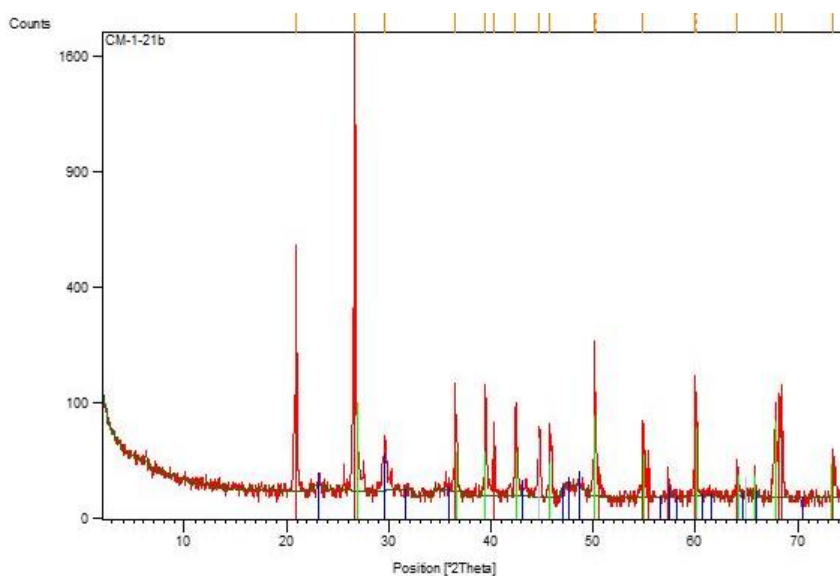|	Quartz	Calcite	Aragonite	dolomite
Protolith	100%	75%	0%	25%
Fault	100%	100%	0%	0%
Damage Zone	100%	33%	67%	0%

Figure 25. XRD analyses from the fault surface at meter 21. Green peaks represent quartz and blue represent calcite. These are the same peaks for other areas where quartz and calcite are present.
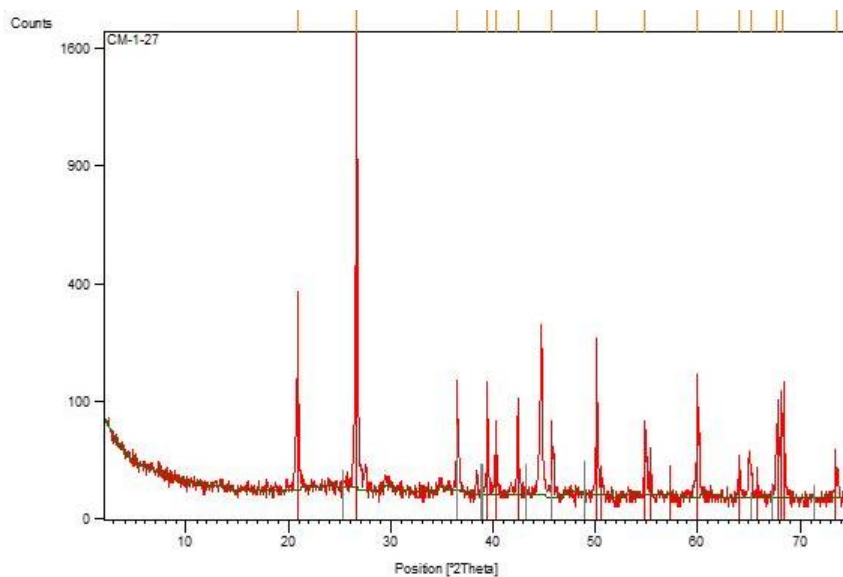
Figure 26. XRD analyses from the damage zone at meter 27. Red peaks represent quartz and gray represent aragonite. These are the same peaks for other areas in the damage zone where quartz and aragonite are present.
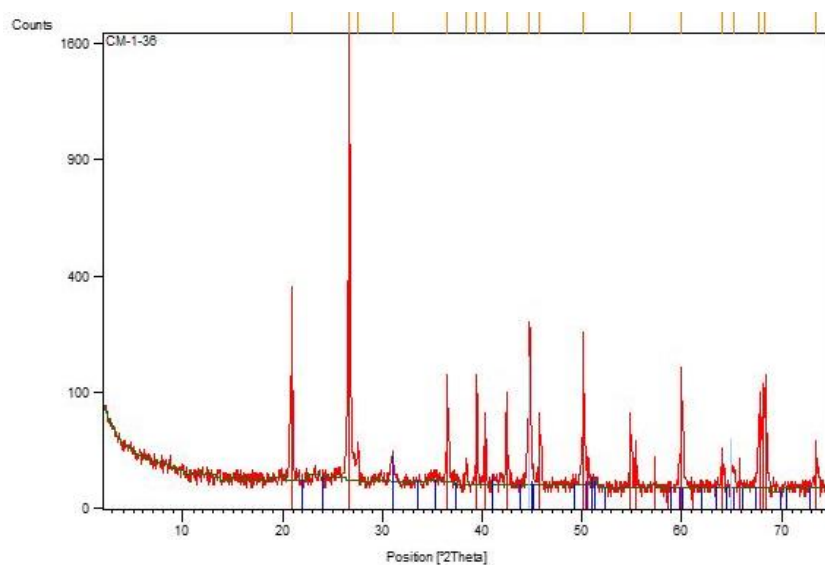

Figure 27. XRD analyses from the protolith host rock outside the damage zone at meter 36. Red peaks represent quartz and blue represent dolomite.

3.1.5 F1 Thin-Section Petrography

Thin section analysis enables us to examine the mineralogy and petrographic

relationships between the different rock types. The protolith sandstone consists of sub-

angular to sub-rounded quartz grains with a feldspar content of 1 to 2 % (Figure 28).

Some of the feldspars (Figure 28) exhibit kaolinite rims around the grains. Kaolinite is

also present in some of the matrix between grains in various thin sections (Figure 28c),

likely a result of alteration during diagenesis or due to grain to grain collisions (Mack,

1978). These processes contribute to significant losses in total feldspar (Mack, 1978).
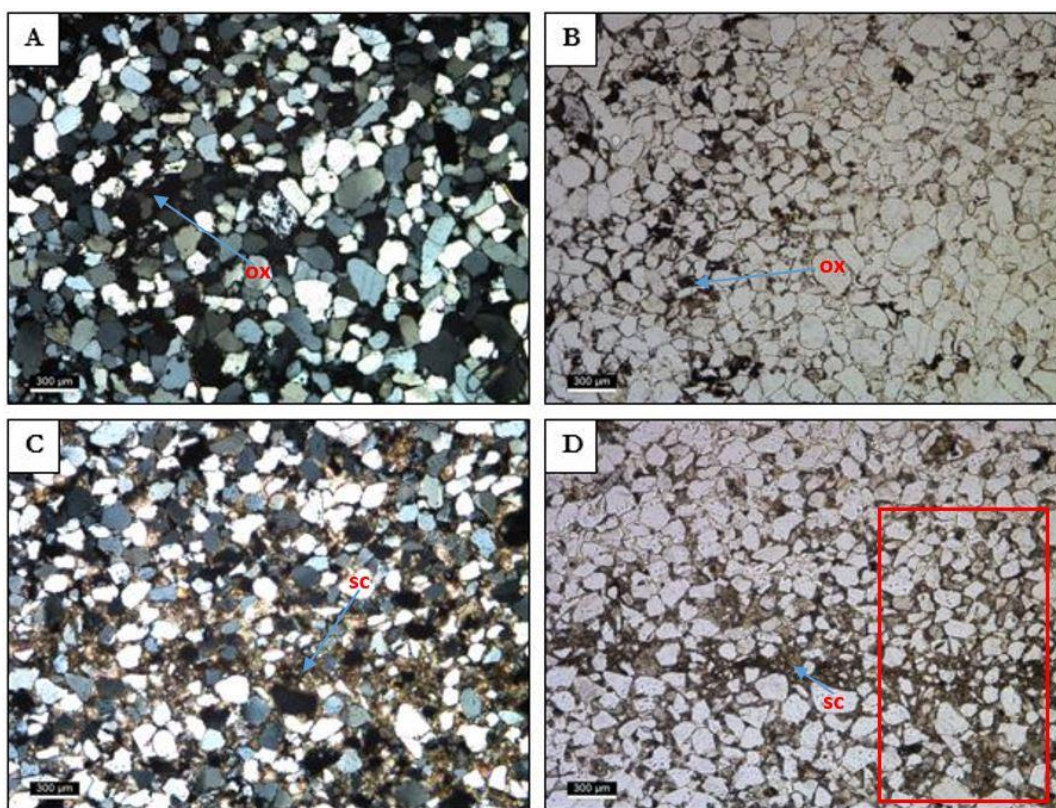

Figure 28. Thin section selections from F1 damage zone. A) Cross polarized view and B) plane polarized view. C and D are the same thin section. Iron oxide mineralization (ox) is pointed out in images A and B. Sparry calcite mineralization (sc) a fracture is pointed out in images C and D. The red box on image D outlines an area where cataclasis can be seen.

3.2 Fault F2
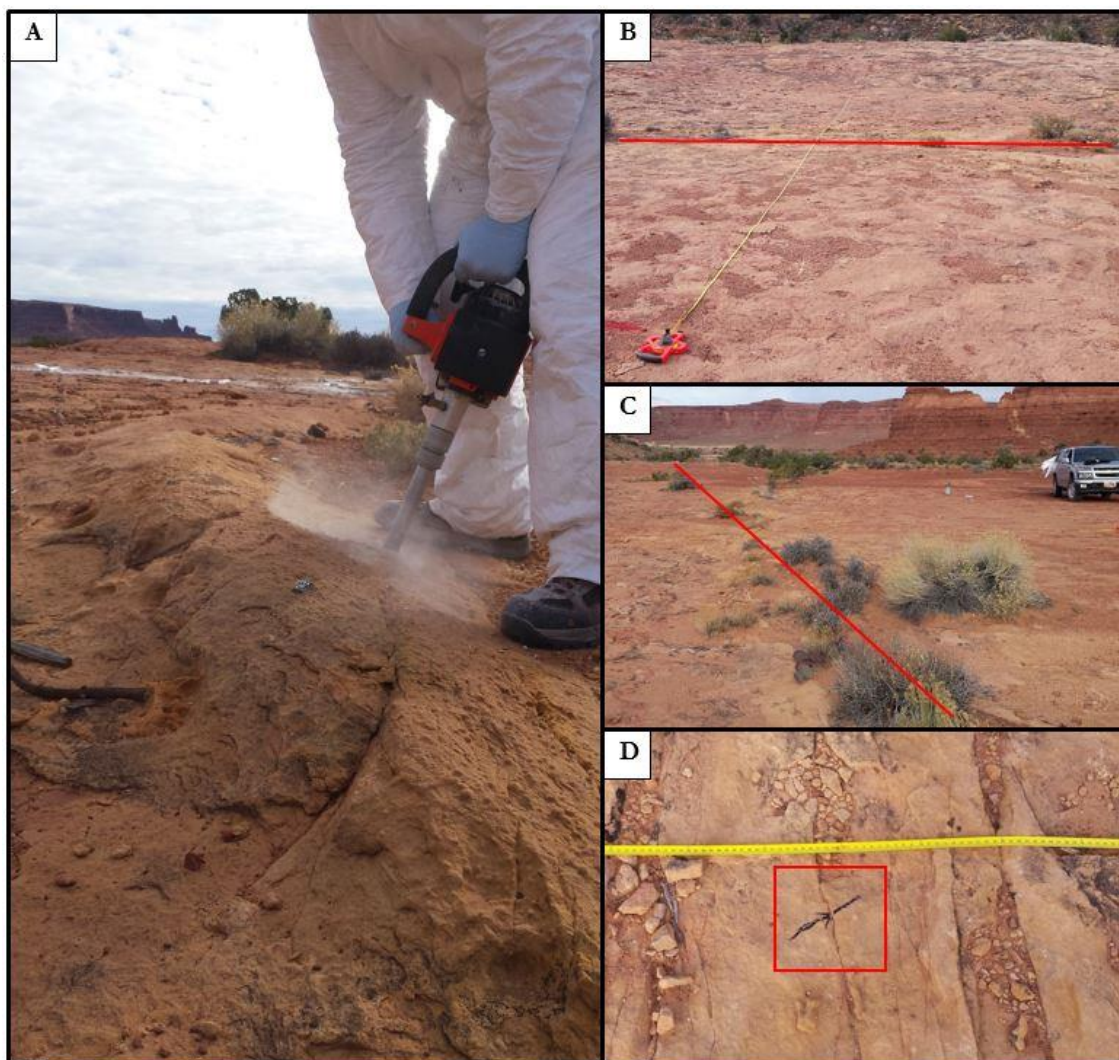
Figure 29. Site F2 overview. Images A through D all show various areas of site F2. Red lines indicate the strike of the fault and the red box outlines north orientation in image D. The red line on image C shows the orientations of Fault F2. Images B and D show the scan line set up at this location with the red line indicating the fault. Image D shows a fracture in the damage zone near the fault surface with orientation of north encircled by a red box.
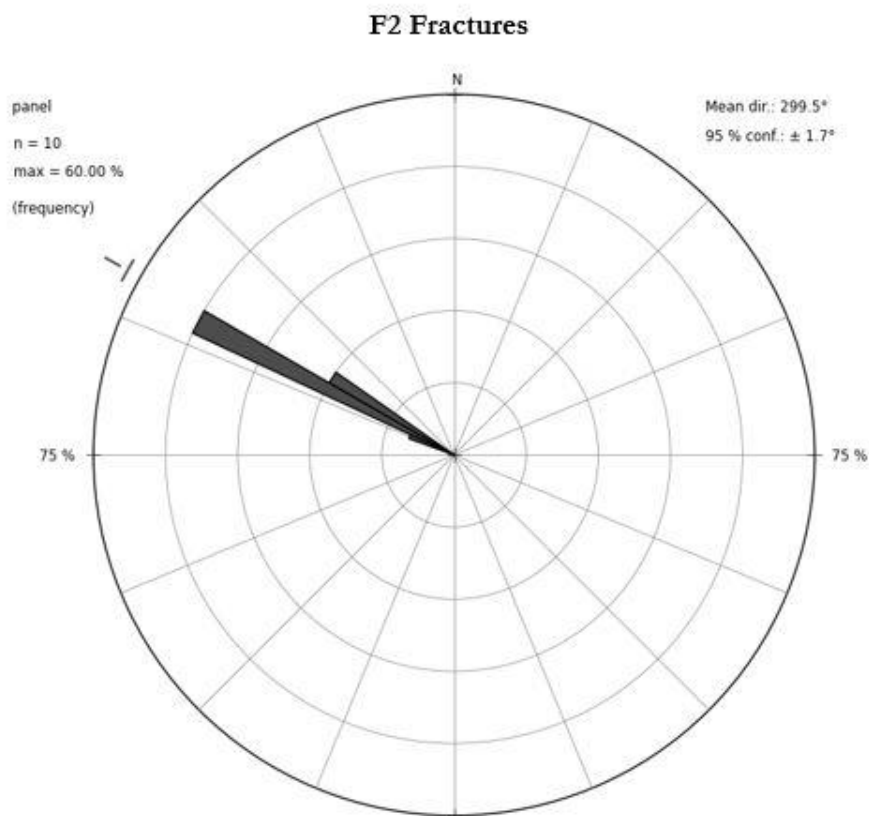
Figure 30. F2 fractures rose diagram. Rose diagram created using OpenStereo showing orientation of 10 fracture sets present near Fault F2 which has a trend of 306 degrees.

This fault has approximately 0.25m of displacement, and is the lowest offset end member analyzed. The linear scan line is oriented perpendicular to Fault F2 (Figure 29B).

3.2.1 Fault F2 Orientation and Fracture Analysis

Fault F2 is oriented 306°/81° SW. The damage zone was measured at approximately 4 meters wide. Numerous fractures are found in the damage zone of Fault F2. The majority of fractures present in this outcrop are parallel to the fault surface shown in Figure 29D and also exhibit similar dips to that of Fault F2.

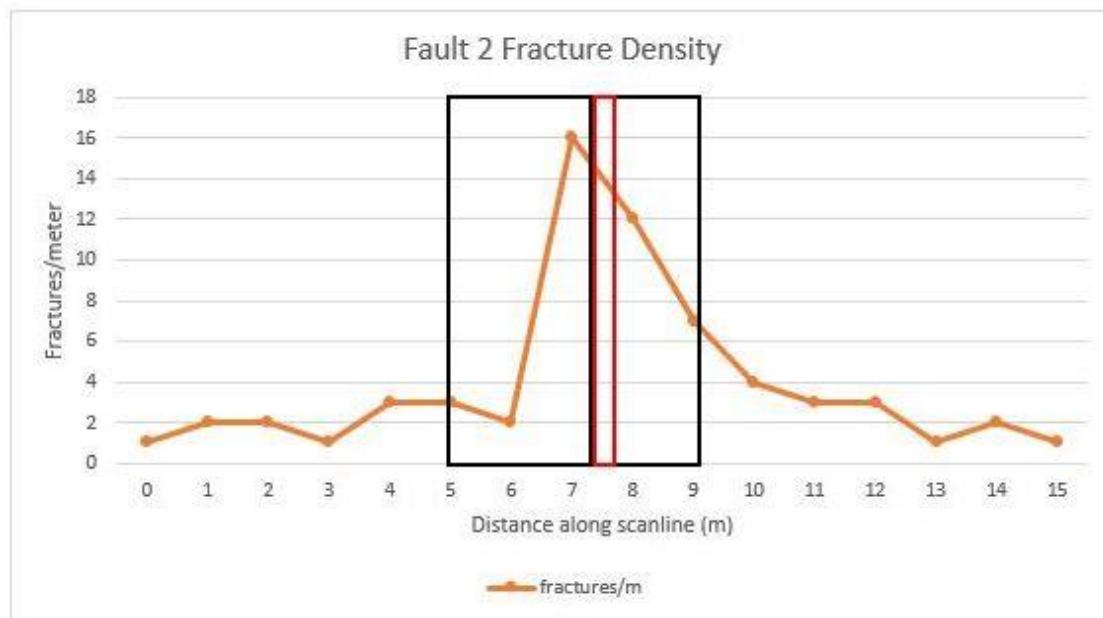Figure 31. Fracture density graph across Fault F2. Fractures are displayed in fractures per meter. The Black boxes outline the damage zone and the red box outlines the fault surface/core. Outside the black boxes is the protolith zone.

The fault surface occurs at meter 7.5 of the scan line. This fault surface/core is seen in outcrop and is surrounded by a zone of high fracture density and low permeability. The damage zone surrounding Fault F2 in seen from meter 5 up to the fault surface at meter 7.5 and then from meter 7.5 to meter 9. At 0 m and 15 m the fracture density decreases to about 1 fracture per meter. Note the Cedar Mesa Sandstone protolith has a background fracture density of about 1 fracture per meter. Due to this observation, it was determined that at 0m and 15 m along the scan line we were in protolith sandstone.

3.2.2 F2 Permeability
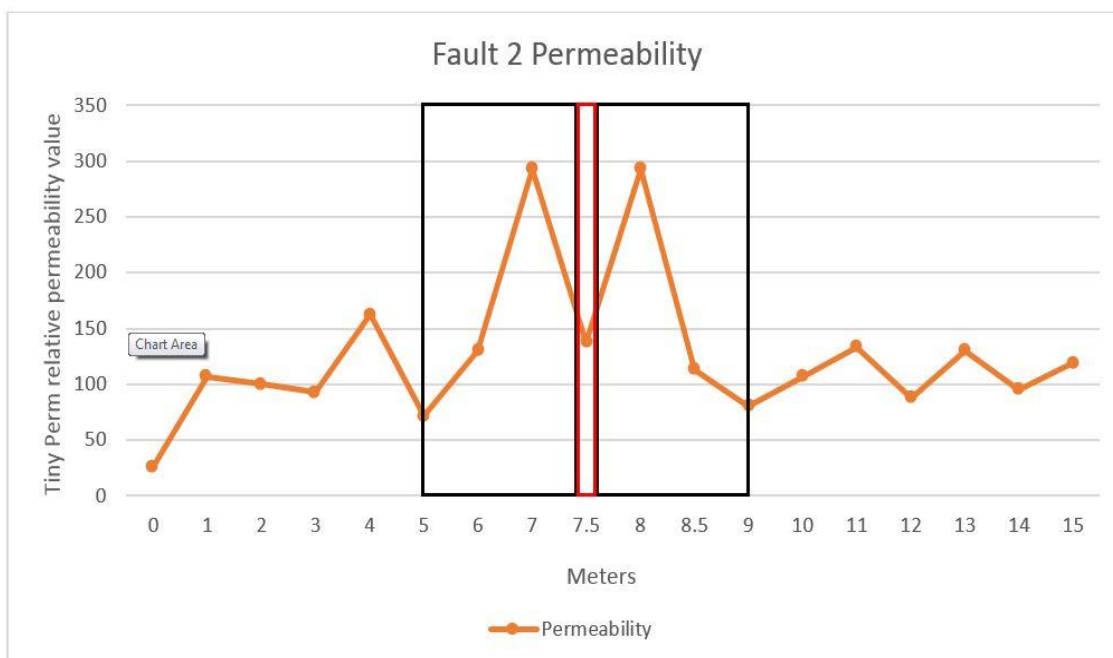
Figure 32. Permeability measurements across Fault F2. Black boxes outline damage zone and the red box outlines to fault surface/core. Outside the black boxes is the protolith zone. The exact fault surface occurs at 7.5 meters.

Relative permeability increases within the damage zone to as much as 3 times the average in the host rock in the damage zone to the southwest of the fault surface starting at about 5 meters to 7 meters and then drops at the fault surface before increasing to above average again in the damage zone to the northeast of the fault up to meter 9 (Figure 32). Outside the damage zone the permeability increases and decreases are most likely due to the corresponding changes in fracture density at these locations along the scan line.

3.2.3 F2 X-Ray Diffraction Analysis

Six whole-rock samples from this fault including two from each zone one on either side of the fault surface were analyzed using X-ray diffraction to determine the major rock-forming minerals. As a whole all three faults had samples which contained different combinations of quartz and carbonates. The only carbonate picked up by the XRD in F2 was dolomite. Quartz is in every sample and has the greatest peak intensity. Dolomite is found in samples from protolith, fault surface, and damage zone. Some samples are void of carbonate according to the XRD analysis. This was not the case when the thin sections were analyzed. Calcite fills the small fractures present in area F2. Samples for F2 were collected with a core drill and were much smaller than F1 samples
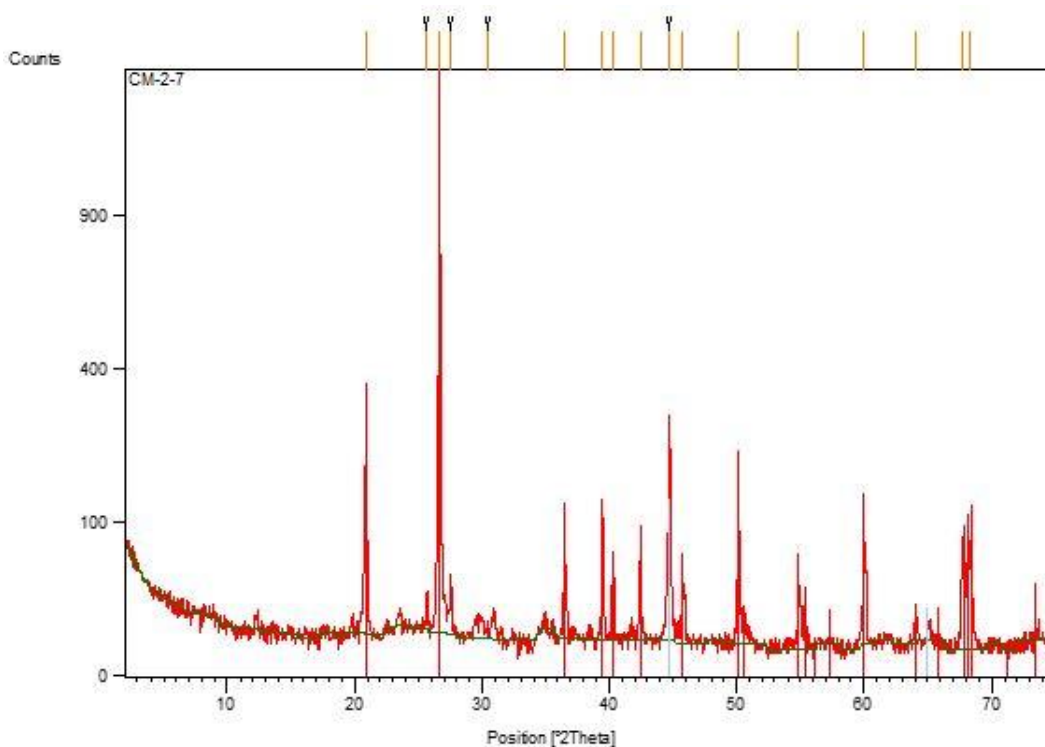

Figure 33. XRD analyses from near the fault surface at meter 7 F2. Red peaks represent quartz.
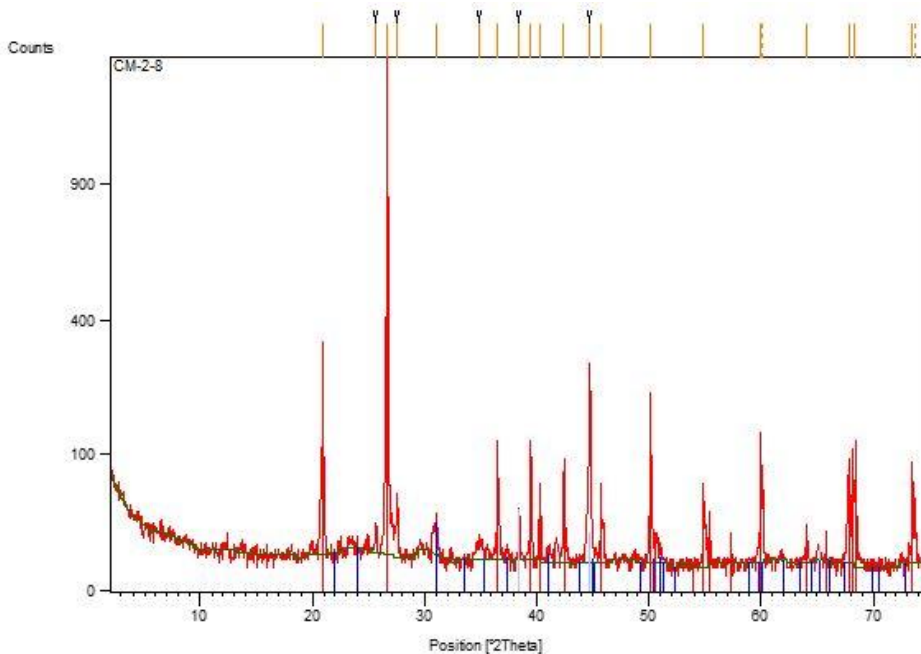
Figure 34. XRD analyses from near the fault surface at meter 8 F2. Red peaks represent quartz and blue represent dolomite.

3.2.4 F2 Thin-Section Petrography
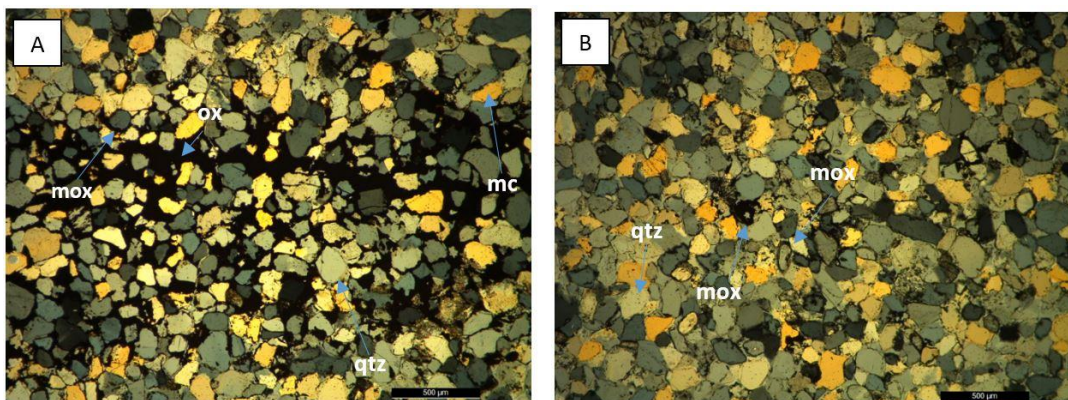
Figure 35. F2 thin sections under polarized light. Photomicrographs from samples located along the linear scan line across Fault F2. Image A is an image of a sample of Cedar Mesa Sandstone from the damage zone which contains a fracture that has been infilled by iron oxide. Arrows in the image point out the iron oxide (ox), quartz grains (qtz), quartz grains surrounded by micritic iron oxide borders (mox), and quartz grains surrounded by micritic calcite boarders (mc). Image B is a sample of Cedar Mesa Sandstone from the protolith zone that contains quartz grains (qtz) along with some iron oxide mineralization (ox) and also quartz grains surrounded by micritic iron oxide borders (mox).
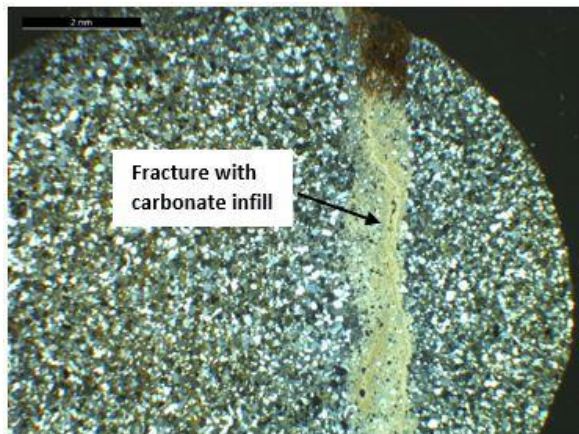
Figure 36. Calcite or dolomite filled fracture from site F2. Quartz grains dominate the field of view on both sides of the fracture.
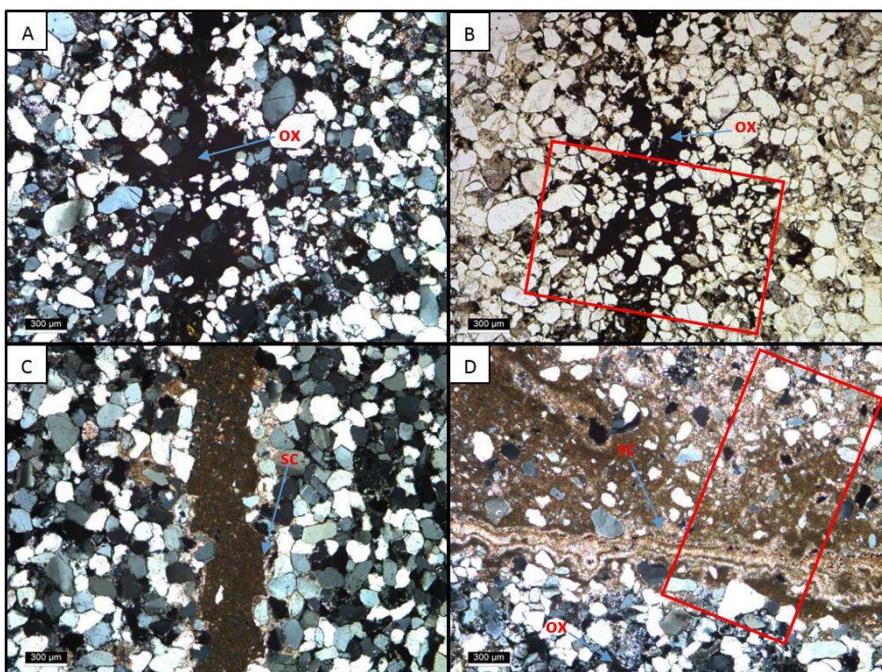
Figure 37. Select thin sections from F2 plain light versus polarized light. Images A, B, and D are from the damage zone and mage C is from the protolith zone. Images A, B, C, and D all show various fractures present at site F2. Images A and B are the same image under different lighting styles. Images A, B, and D are good examples of cataclasis seen in site F2. Red boxes in images B and D show areas were cataclasis can be seen. From the three thin sections shown in images A, B, C, and D multiple types of mineralization can be seen in the fractures. Images A and B show iron oxide mineralization (ox) while images C and D show sparry calcite mineralization (sc).

A total of 19 samples were collected at site F2 using a hand held core drill. Thin

sections were created from each of these samples. Figure 36 shows the same fracture

illustrated in in image D of Figure 37 at lower magnification.

3.3 Fault F3
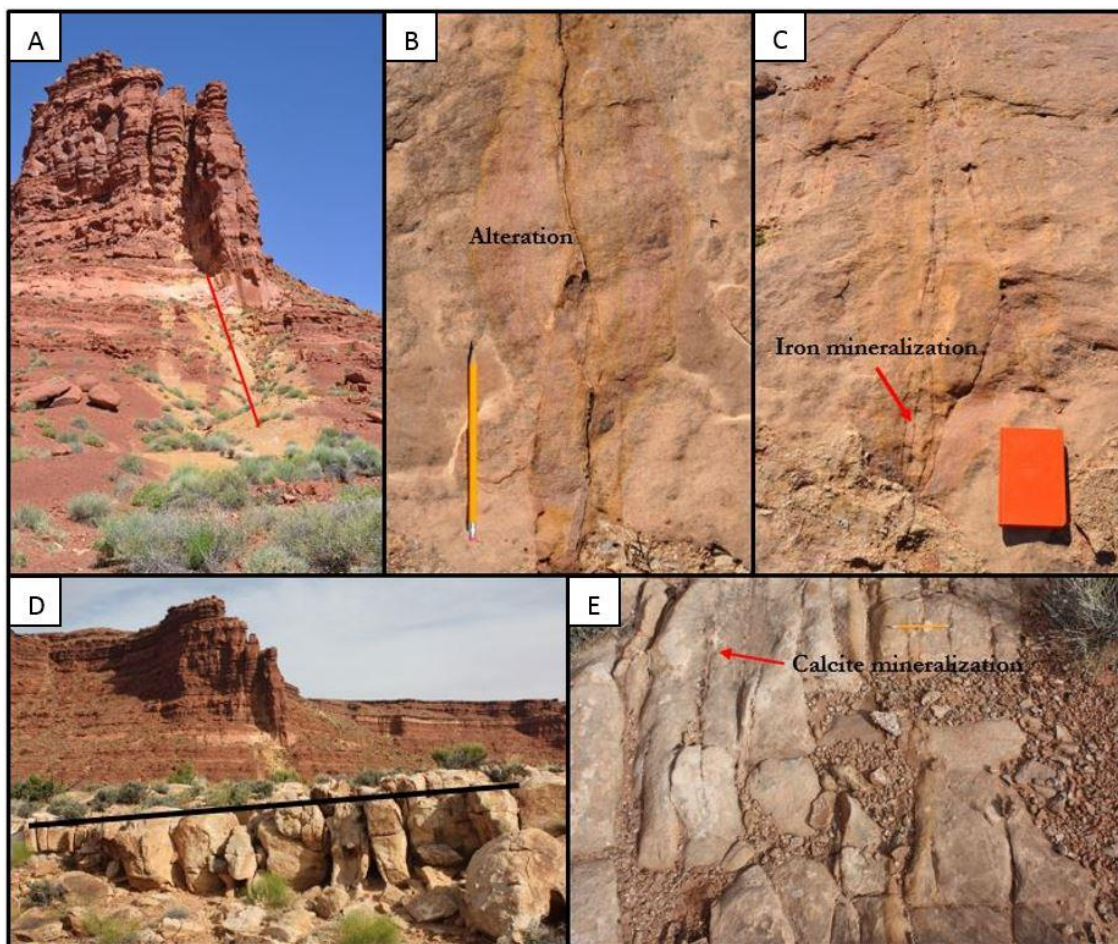
Figure 38. Site F3 overview. Site F3 includes a fault with an average displacement of approximately 2 meters. Images A through E all show various areas of site F3. Images C and E show different types of mineralization present. In image C fractures can be seen mineralized by iron and in image E fractures have been mineralized by calcite. In both images C and E alteration can be seen in the rock as well. The alteration in most easily seen in image B where it is very prominent.

Fault F3 has about 2 meters of displacement, of the 34 faults measured in the study area (Figure 9) this fault has a displacement which is approximately equal to the average. Fault F3 cuts through the overlying Organ Rock Formation, easily identified by the yellow band of altered rock (Figure 38A). Fault F3 has various types of iron and calcite mineralization which can be seen in Figure 38.

3.3.1 Fault F3 Orientation and Fracture Analysis

Fault F3 strikes at 308° and dips to the southwest at 80°. The displacement of this fault is about 2 meters and the damage zone is 12 meters wide. The majority of the fractures present in this outcrop run parallel to the fault surface (Figure 39). Almost all of the fractures have similar dip to that of Fault F3. Along this scan line orientations of 16 main set of fractures were measured which are plotted in Figure 39 below. There are multiple fracture sets that do dip in the opposite direction of Fault F3 to the northeast which did not intersect the scan line.

In Figure 40 fracture densities associated with Fault F3 show a significant increase near the fault surface/core. The fault surface occurs at meter 16.5 of the scan line. The damage zone surrounding Fault F3 in observed from meter 10.5 up to the fault surface at meter 16.5 and then from meter 16.5 to meter 22.5. At 0m and 36m the fractures per meter decrease to between 2 to 5 fractures per meter. This is higher than the 1 fracture per meter protolith of the other two faults. Based on field observations and taking into account other parallel faults in the area it was decided that this was indeed protolith Cedar Mesa sandstone. The only other option is that the scan line should have extended slightly further in the 0 direction.
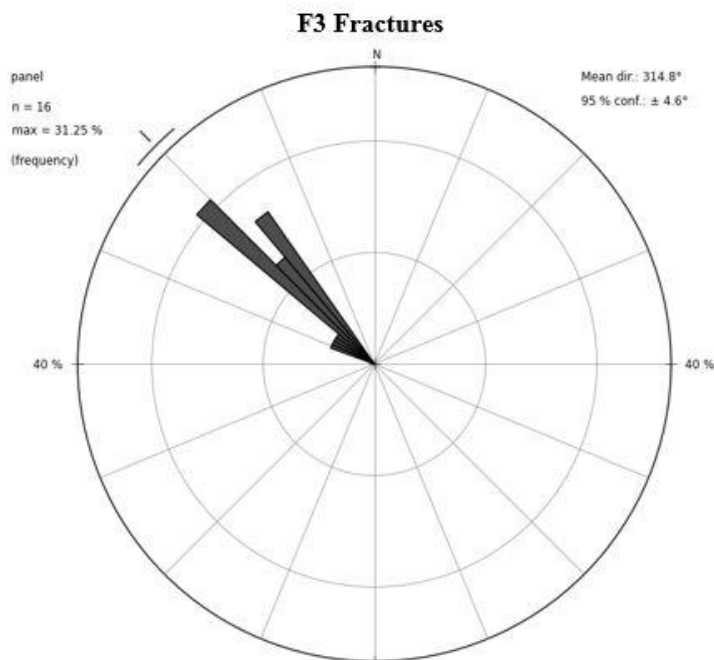
Figure 39. Rose diagram of fractures from F3. Shows orientation of 16 fracture sets present near Fault F3. Created used OpenStereo
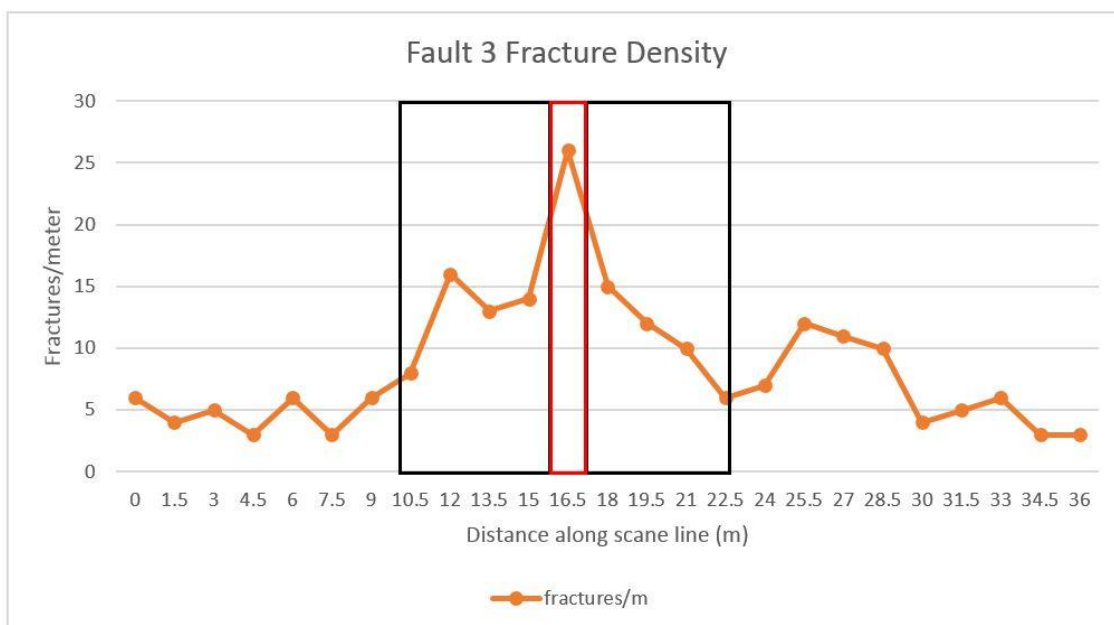
Figure 40. Fracture density graph across Fault F3. In this figure the black boxes outline the damage zone and the red box outlines the fault surface/core.

3.3.2 F3 Permeability

The permeability measurements at this fault do not have much correlation due to outliers in the data, like the one at 4.5m (Figure 41). With the amount of spikes and low measurements this data is not as useful for making inferences as permeability data from the other 2 faults. Permeability measurements were taken at this location on a separate trip from the other two fault locations. After this trip the TinyPerm tool was sent in for work and calibration. Due to this as well as the amount of outliers and abnormalities I discount this data.
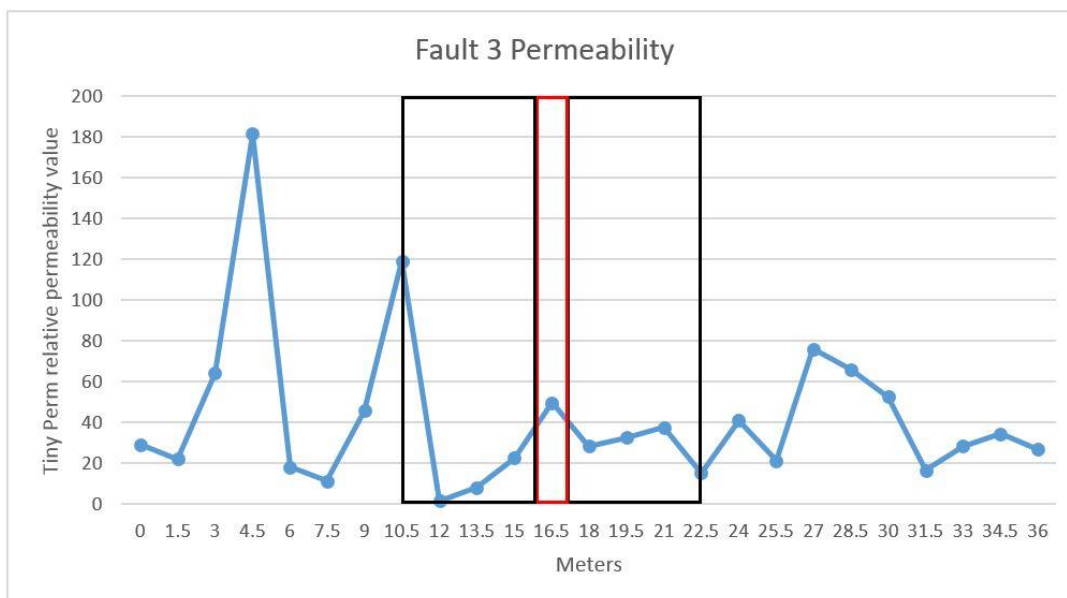
Figure 41. Permeability graph across Fault F3. In this figure the black boxes outline the damage zone and the red box outlines the fault surface/core.

3.3.3 F3 X-Ray Diffraction Analysis

Intact samples for F3 where used to create thin sections. The XRD data does not exist for this fault due to heavy contamination by drilling fluids during sample collection.

3.3.4 F3 Thin-Section Petrography

Thin sections were made for 24 samples collected from site F3. Each sample was collected using the hand held core drill. Of those 24 samples multiple were destroyed and not useable for petrography.

These thin sections from along Fault F3 were made from samples collected in the damage zone of fault F3. Image C highlights one of the alteration halos similar to that seen in Figure 38 image B. Sparry calcite and clay are identified in this alteration halo. Based on the XRD results from F1 and F2 this is likely kaolinite. Some original feldspar grains have altered into the kaolinite grains seen within the alteration halo areas (Figure 42).
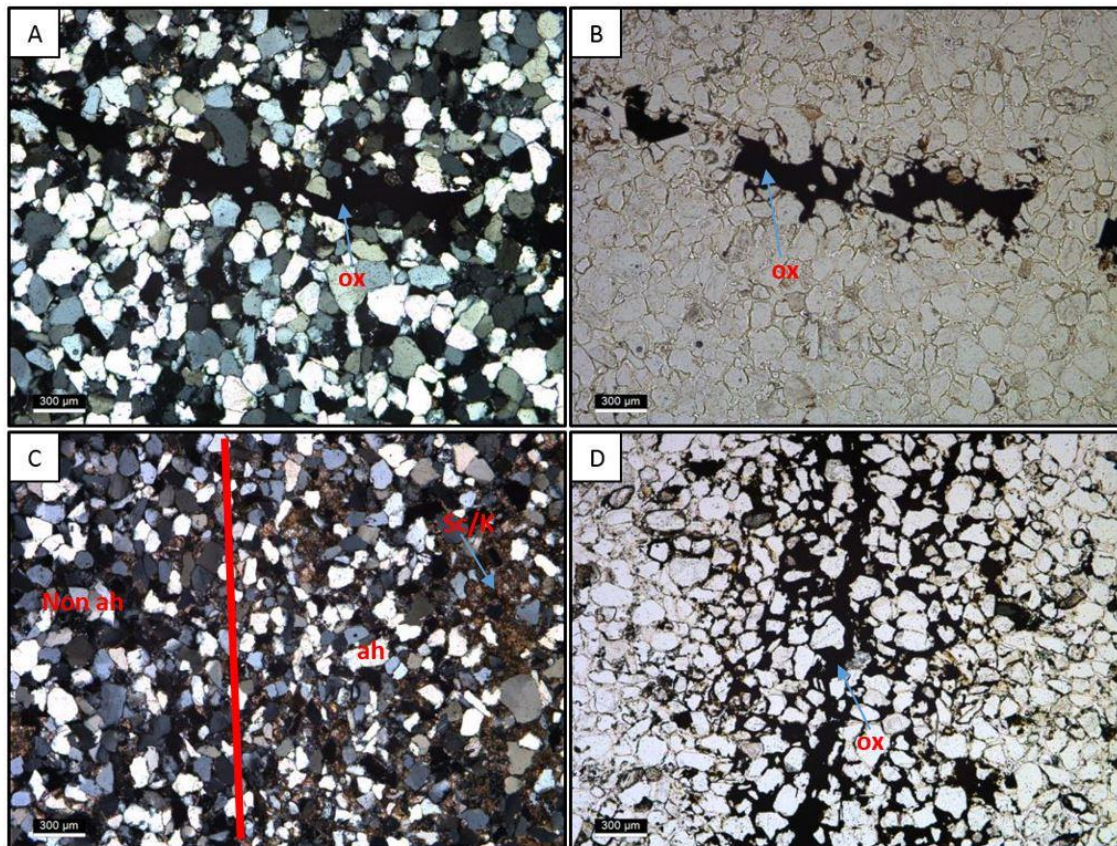
Figure 42. Select thin sections from F3. Images A, B, C, and D show various fractures that have been infilled with iron oxide (ox). Image C shows possibly sparry calcite and kaolinite (Sc/K). Also in image C a red line divides the area into a non-alteration halo zone and an alteration halo zone. Images A and B are the same thin section. Image A is viewed with cross polarized light and image B is viewed using plain polarized light. In plain light the extent of the iron oxide mineralization can be more easily recognized. In this sample the iron oxide has mineralized in a fracture that was sampled in the core. In all three faults studied alteration halos are present around many of the fractures. Image C shows the edge of one of these alteration halos. To the right of the red line in image C an alteration halo can be seen. This same alteration halo can be seen in hand sample and was chosen as a location for a thin section. To the right of the line the pore spaces are filled with what may be clays from alteration or iron oxide that has been mineralized in the pore spaces.

3.4 Ultra Violet Photography

Figure 43. UV photo comparison F1. Plain light versus UV light photographs of fractures near Fault F1 in the Hite field area. A lighter with a length of 3 and ¼ inches in length is used for scale in photo A. The main fracture set in this photo has approximately and 305° trend. In this figure the calcite that has been precipitated in the fracture is more easily seen as it fluoresces under UV light. The iron oxide that has mineralized in some fractures does not fluoresce under the UV light.

Figure 44. UV photo comparison F2. Plain light versus UV light photographs of fractures near Fault F2 in the Hite field area. The main fracture shown in this photo has approximately a 306° degree trend. In the plain light photo the calcite is not easily visible, but once illuminated by UV light the calcite fluoresces and if easily identified. A scale of 1.5 feet is given in Image A.
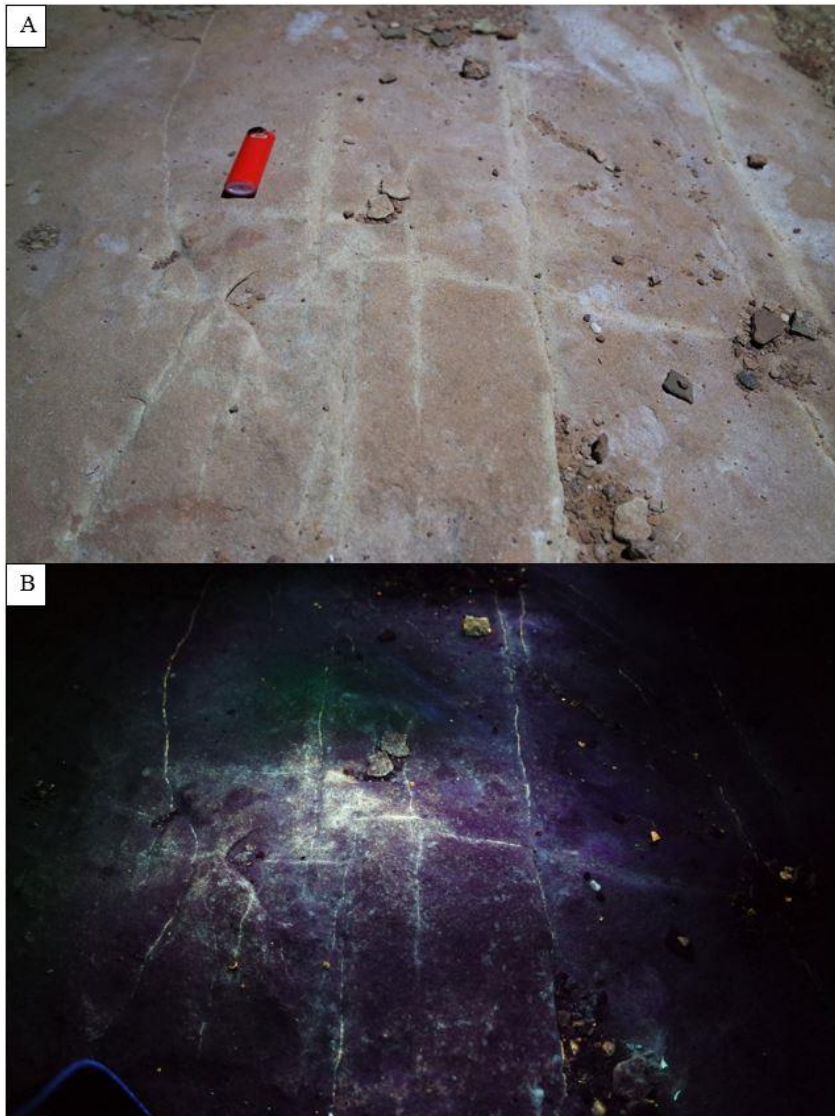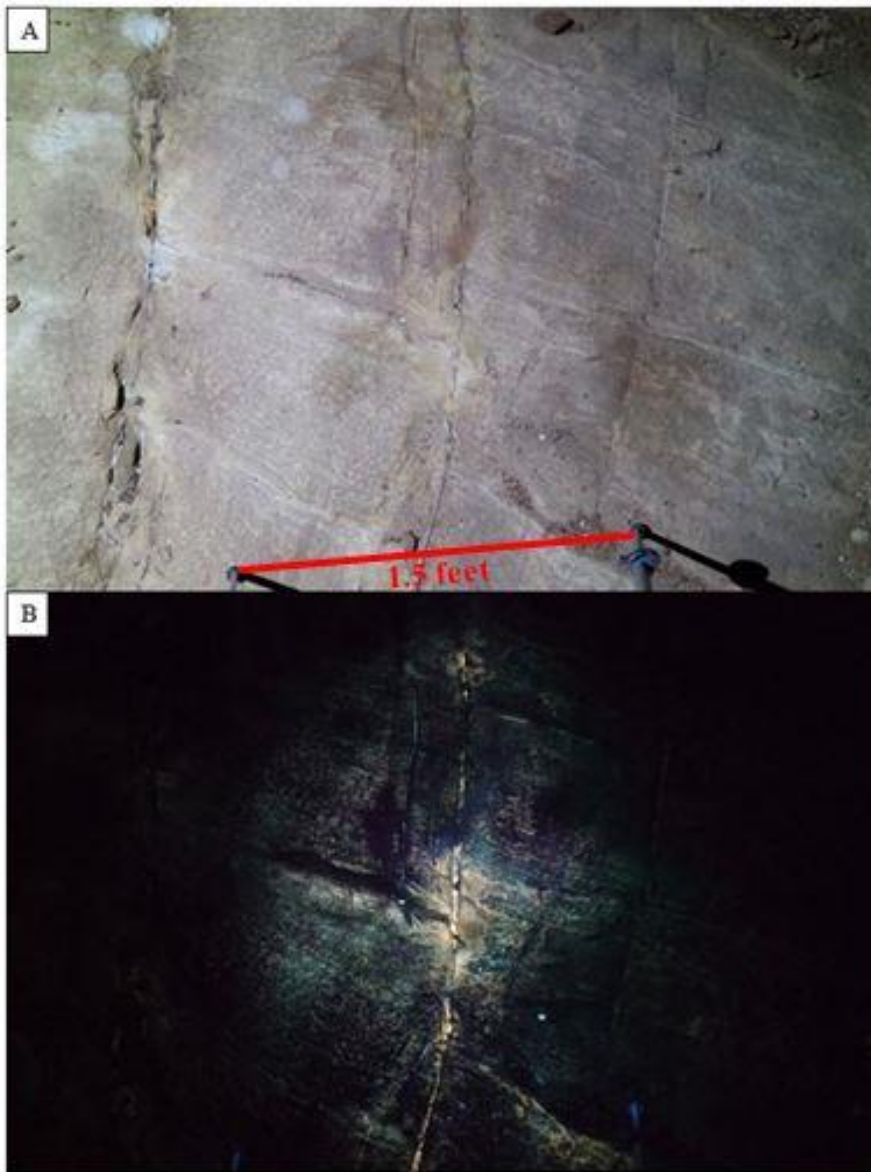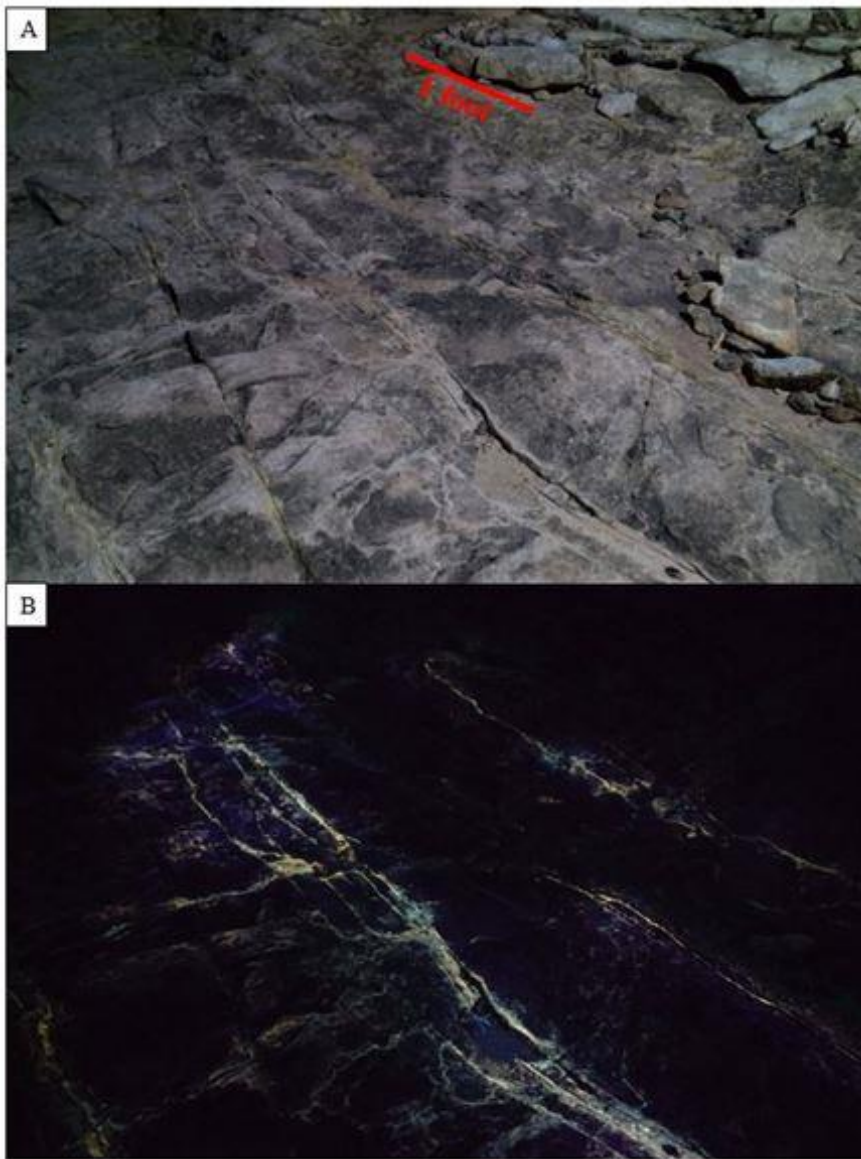
Figure 45. UV photo comparison F3. Plain light versus UV light photographs of fractures near Fault F3 in the Hite field area. The main fracture set in this photo has approximately a 308° trend. In this figure some calcite can be seen in some fractures under plain light, but under UV light it is easy to see which fractures contain calcite and which do not. I scale of 1 foot is given in Image A.

Mesoscopic mineralization patterns are revealed with night time photography of the faults illuminated by ultraviolet light (Petrie et al., 2013; Figures 41, 42, and 43). Various minerals and elements will exhibit fluorescence when they are exposed to an electron, X-ray, or ion (MacRae and Wilson, 2008). In this case this luminescence is associated with short or long wave ultraviolet light. The UV fluorescence is a strong tool for mineral identification but in this study we use UV fluorescence with ultraviolet light to more easily identify crosscutting relationships associated with fault damage zones and deformation bands. Fluorescence likely associated with Ca-rich mineralization along with trace elements such as U and Mn (MacRae and Wilson, 2008; Petrie et al., 2013). Deformation bands in Figure 45 show evidence of mineralization in the fractures near the fault core under UV light. It is commonly thought that deformation bands are associated with low permeability, but in this case it is seen that a fluid precipitated calcite within the deformation band. In the fractures and pore space immediately bordering the deformation band surface calcite is present and fluoresces. Calcite precipitated in open mode fractures readily fluoresces and allows easier visualization of the entire fracture network. In Figures 26, 34, and 35 photomicrographs from faults F1 and F2 show evidence of calcite mineralization in fractures. Calcite precipitation in the open mode fractures is consistent with chemical XRD findings. In Figures 41, 42 and 43 the calcite that is precipitated in the fractures can be more easily seen due to its response to the UV illumination.

CHAPTER IV

DISCUSSION

Three faults with different amounts of offset from the Hite Fault Group were characterized to interpret the relationships between fault zone architecture, fluid flow, and mineralization events. We use the microscopic and mesoscopic observations to determine the relative timing of mineralization. We interpret multiple fluid flow events to be related to initial movement and reactivation of the studied faults. Evidence for various mineralization events can be seen in thin sections taken from the faults and related damage zones. More inferences about the fluid-fault interaction can be made about Fault F1 due to the geochemical analyses that were performed on samples collected here. Although faults F2 and F3 do not have associated geochemical data much can be learned about the fluid-fault interaction from the thin sections and physical data collected from these faults.

4.1 Fault F1

There is much evidence for fluid flow surrounding Fault F1. Bleaching of the sandstone adjacent to the fault in the Cedar Mesa Sandstone and in the overlaying Organ Rock Formation, iron oxide alteration halos surrounding fractures with close proximity to the damage zone and fault surface/core, and calcite and iron oxide mineralization in the fractures of the damage zone and fault surface/core attest to fluid flow. High fracture densities associated with the damaged zone around the fault appear to have acted as migration pathways for subsurface fluids. Fluid migration is expressed by the bleached alteration halos around fractures (Figure 46). Due to the porous and permeable nature of

sandstone the iron oxide rich fluid was able to penetrate into the formation (Figure 14).
These alteration halos of iron oxide minerals represent the degree to which the fluid was
able to migrate into formation. These halos are recognizable due to the contrast between
the bleached sandstone and the coloration of the iron oxide that has been mineralized in
the formation from the iron oxide rich fluid. Permeability data collected in the field
(Figure 17) shows the damaged zone surrounding the fault as having high permeability
even with the remineralization.

Thin sections images from Fault F1 (Figure 28) show evidence for iron oxide
mineralization as well as calcite mineralization in the fractures and pore spaces. Figures
27 C and D show a fracture in which calcite mineralization and cataclasis of host rock
grains have occurred. The iron oxide and calcite mineralization in the fractures appear to
be the result of two separate events. This is based on field observations where calcite is
mineralized in the fracture and is surrounded by iron oxide mineralization and iron oxide
alteration halos (Figure 46). The first type of fluid-flow or alteration event that is
discussed is the iron oxide emplacing event. Two distinct styles of iron oxide alteration
are apparent in the field. The first is the iron oxide alteration within the fracture that does
not penetrate more than a few millimeters from the fracture. The second is the pervasive
iron oxide alteration that creates iron oxide alteration halos that penetrate much deeper
into the host Cedar Mesa Sandstone. Both of these can be seen in Figure 46 below. The
second alteration or fluid-flow event which deposited calcite in the fractures can be seen
in Figure 46 as well. The flow which deposited the calcite also accounts for higher CaO
concentrations in various zones of the Fault F1 scan line. This scan line is where samples

were collected for whole rock geochemistry analyses.   Field data in combination with

data collected in the lab support these observations of at least two fluid-flow or alteration

phases. Thin sections from Fault F2 show more evidence that support this theory. In thin

sections from Fault F2 seen in Figures 33, 34, and 35 open mode fractures and fractures

with a component of shear can be seen, both which exhibit different forms of alteration or

mineralization and movement.
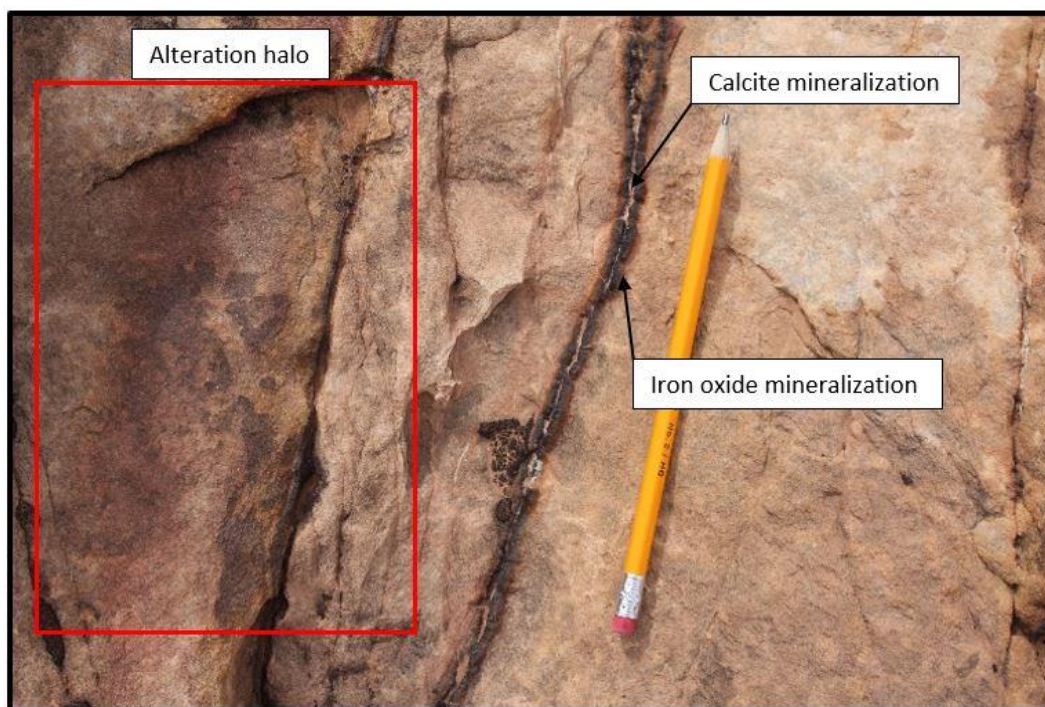
Figure 46. Image of fractures from fault F1. Iron oxide and calcite mineralization can be
identified in this figure. An example of an alteration halo around one of the fractures is
also outlined in this image.
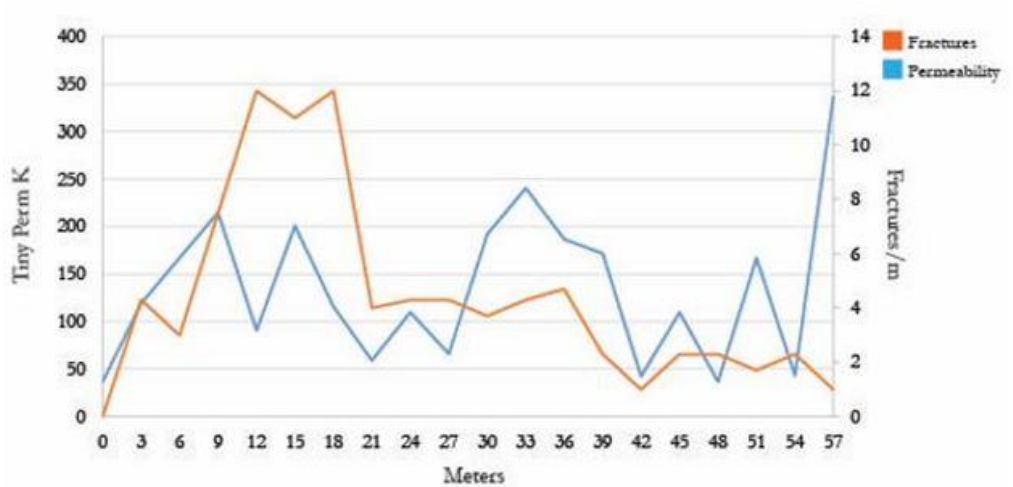
Figure 47. Fracture density and permeability graphed against distance across Fault F1 without geochemical data included. This figure shows how the permeability and fracture density data compare to each other along the scan line set up at Fault F1.
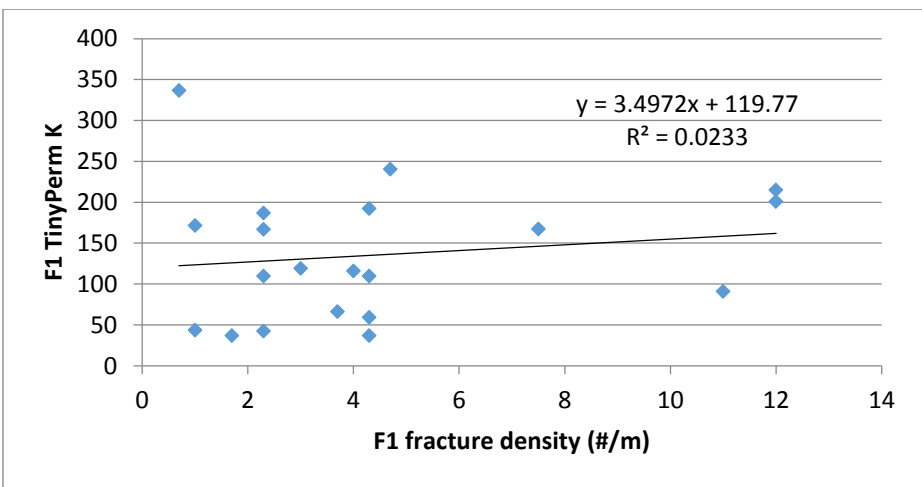
Figure 48. Fracture density and permeability cross plot F1.

We might assume that permeability should increase as fracture density increases in the traditional fault model (Caine et al., 1996), and this data does agree with this as shown in Figure 48 there is a linear trend in the data. In some areas along the scan line it

looks like the data plotted in Figure 47 do not mimic each other, but in other areas the permeability and fracture density data do correlate. This general relationship between fracture density and permeability is shown in Figure 48. The damage zone in the fault ranges from meter 6 up to the fault surface at meter 21 and then continues to meter 33 on the other side of the fault surface. At meter 21 where the fault surface is present the permeability and the fracture density drop. In the damage zone the lines plotted from the data move inversely to each other.

During field work and initial analysis I theorized that damage zones with areas of high fracture density should exhibit high permeability due to the possible open space in the fractures. Data for Fault F1 begins to show that this general relationship is valid. The trend in the data is not as strong as I assumed it would be initially, but there may be some influences on this that can be seen in the data. In the damage zone we see fractures that are mineralized with iron oxide and calcite. The iron oxide is mineralized on the outer edges and calcite in the interior of the fractures. Open space created by open mode fractures which would greatly increase permeability has been infilled by precipitation of calcite causing only a slight increase in permeability.

4.1.1 Whole Rock Geochemistry

Whole rock geochemistry was performed on 19 samples for Fault F1 and the whole-rock geochemistry combined with fracture and permeability data for Fault F1 show that there is an increase in major oxide concentrations and decreases in fracture density and permeability (Figure 19). The damage zone defined by the fracture densities (Figure 17) ranges from meter 6 to meter 33 on either side of the fault surface. A decrease

in abundance of major oxides corresponds to an increase in fracture density (Figure 19).

At meter 15 the fracture density is increased but weight percentages of pertinent major

oxides are decreased. This is also seen at meter 33. It is also seen from Figure 19 that

fracture density and permeability are inversely related. This inverse relationship can be

seen at meter 12 in Figure 47 where fracture density spikes and the permeability

decreases. In the field fractures have been infilled with calcite and iron oxide which can

be seen in Figure 14. This infill by calcite and iron oxide reduces the permeability by

decreasing the pore spaces available. It is likely that these curves would have mimicked

each other before the pore space was filled by mineralization of various minerals. At this

point we see the curves as they are post mineralization.

When viewing the photos produced with UV illumination along with the whole-

rock geochemistry data some areas fluoresce heavily while others do not. The areas

where the deformation bands and associated fracture networks fluoresce correspond with

areas higher in major oxides concentrations. There is an increase in major oxides from

meter 15 to meter 24 on Fault F1 (Figure 19), especially elevated calcium oxide (CaO) in

this region (Figure 19). The range from meter 15 to meter 24 falls mostly within the

hanging wall damage zone and the fault core. This calcium oxide fluoresces strongly

under short and long wave UV light (MacRae and Wilson, 2008) thus allowing us to see

the fracture networks easily in UV photos of the area. This means that at the same time

that open mode fractures were created in the damage zone a CaO rich fluid was

mobilized and precipitated calcite in the open space of the fractures.

4.2 Fault F2

Field and thin section analyses from Fault F2 show multiple types of fractures associated with the fault (Figures 33, 34, and 35). Open mode fractures containing calcite fill can be observed as well as cataclasic deformation band style fractures containing calcite and or iron oxide fill. The open-mode fractures are superposed on the cataclastically formed deformation bands, providing evidence that agrees with the previously proposed idea of second phase or movement or an extensional reactivation of these faults. In the initial phase of movement there was deformation band style movement. In this phase there was some amount of slip along the fractures. This was not purely extensional movement due to a sense of shear that caused cataclasis, as observed in the thin sections (Figure 37). Images A and B show the first phase of movement where there was a sense of shear that caused cataclasis. At this same time during the first phase of movement the fractures were mineralized by iron oxide (Figure 37 A, B).

Deformation bands are commonly found in rocks with high porosity that can allow space for grains to be physically altered via cataclasis (Aydin and Johnson, 1978; Antonellini and Aydin, 1994; Shipton et al., 2002; Fossen et al., 2007; Dockrill and Shipton, 2010). It is also proposed that deformation band faults exhibit low porosity and permeability (Antonellini and Aydin, 1994; Shipton et al., 2002; Fossen et al., 2007; Dockrill and Shipton, 2010) such that it is unlikely that the iron oxide in the cataclasis precipitated in the deformation band post-deformation. Therefore I suggest that the iron oxide rich fluid must have been present in the fractures at the time of the initial

movement and or migrated in pathways directly adjacent to the deformation bands themselves.

Evidence for the second phase of movement can be observed in Figure 37 C and D. This is an extensional phase of movement or subsequent movement which reactivated the faults in an open mode allowing the development of open mode fractures. During this second phase of movement calcite rich fluid mineralized fractures. Left behind is a sparry calcite filled fracture with isolated cataclasic grains floating in the vein mineral. Adjacent to the fractures iron oxide can still be observed in the host rock. This residual iron oxide from the first phase of movement and mineralization can be seen and is labeled in images C and D in Figure 37.
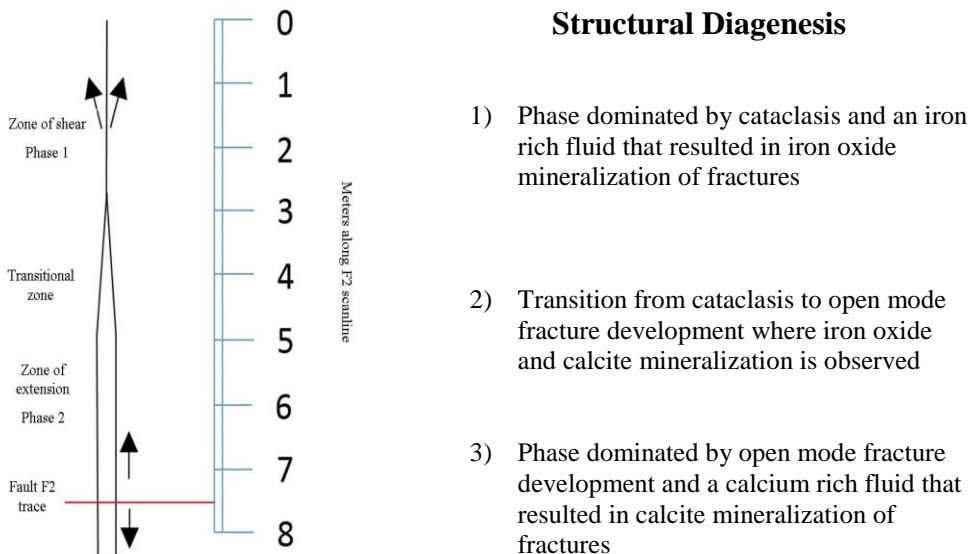

Figure 49. Fault F2 phases of movement. Outline of the Fault F2 scan line and fault location with zones indicating phases of movement and related structural diagenesis. Phase 1 infers the phase of movement when there was a sense of shear causing cataclasis accompanied by iron oxide mineralization. Phase 2 infers an extensional reactivation phase for the faults accompanied by calcite mineralization.

Textures and evidence for mineralization from the first phase of fault movement can be seen in thin sections from meter 2 along the scan line from Fault F2. Textures and mineralization from the second phase of movement can be seen at meter 3 and meter 5 along the scan line from Fault F2 (Figure 49). Based on field observations as well as fracture and permeability data (Figures 29 and 30) the damage zone for Fault F2 starts at about meter 5 of the scan line. The fault surface is at meter 7.5 and the damage zone then continues to meter 9 on the other side of the fault. Fractures associated with the damage zone area are where evidence for the second phase of movement is observed.
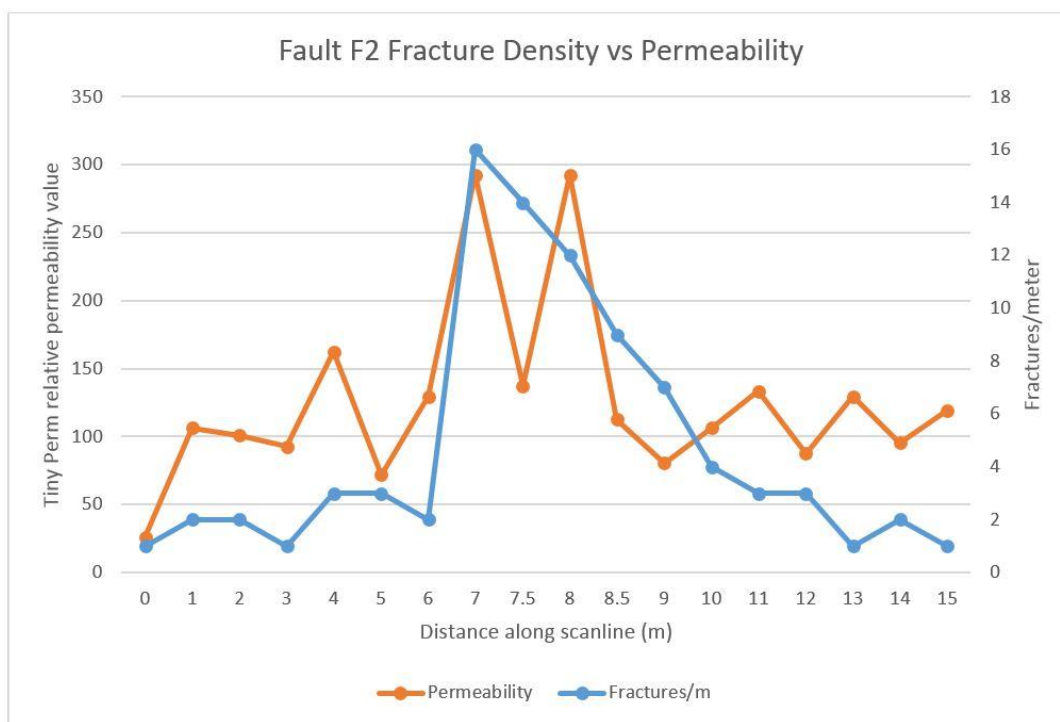

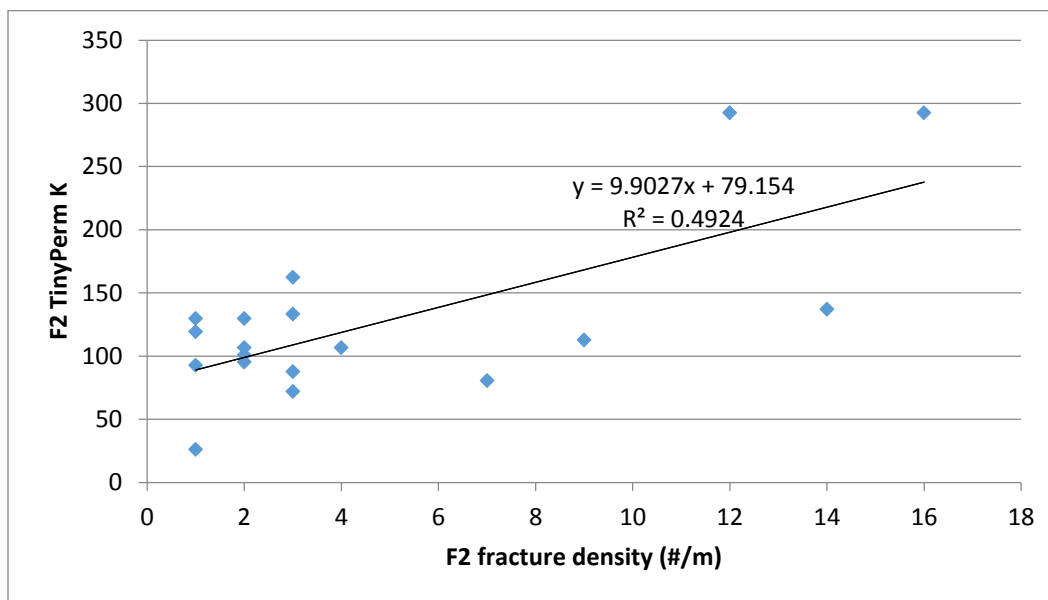Figure 50. Fracture density plotted against permeability for Fault F2.

Figure 51. Fracture density and permeability data for Fault F2. This figure shows that there is a general relationship that relates the fracture density and the permeability data from Fault F2.

Similar to Fault F1 it is inferred that with an increase in fracture density permeability should increase as well. The permeability data for Fault F2 correlate more with this hypothesis than data from the other two faults (Figures 48 and 49). The fracture density is highest in the damage zone in Fault F2 and the permeability is also the highest here. In the damage zone we see fractures that have iron oxide mineralization as well as calcite mineralization. This possibly relates to reactivation where an extensional phase of movement created open mode fractures in the damage zone seen in Figure 49. The damage zone associated with Fault F2 was very uniform in width on either side of the fault surface. Fault F2 was also the fault with the least amount of throw and on the most even topography. These factors made it easier to collect very detailed data along the scan line for Fault F2.
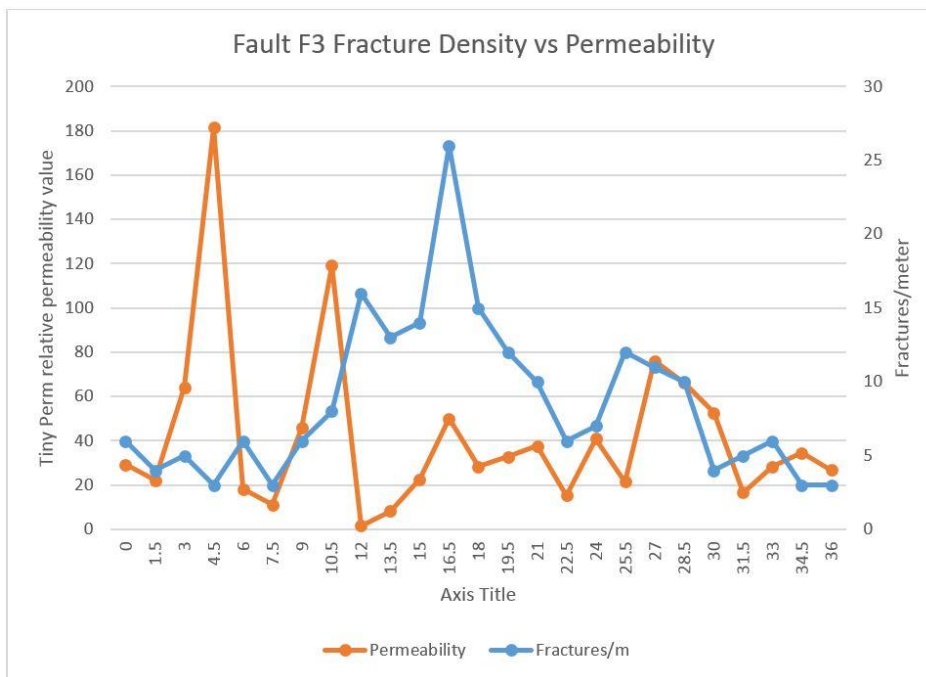
4.3 Fault F3

Figure 52. Fracture density and permeability as a function of distance across Fault F3.
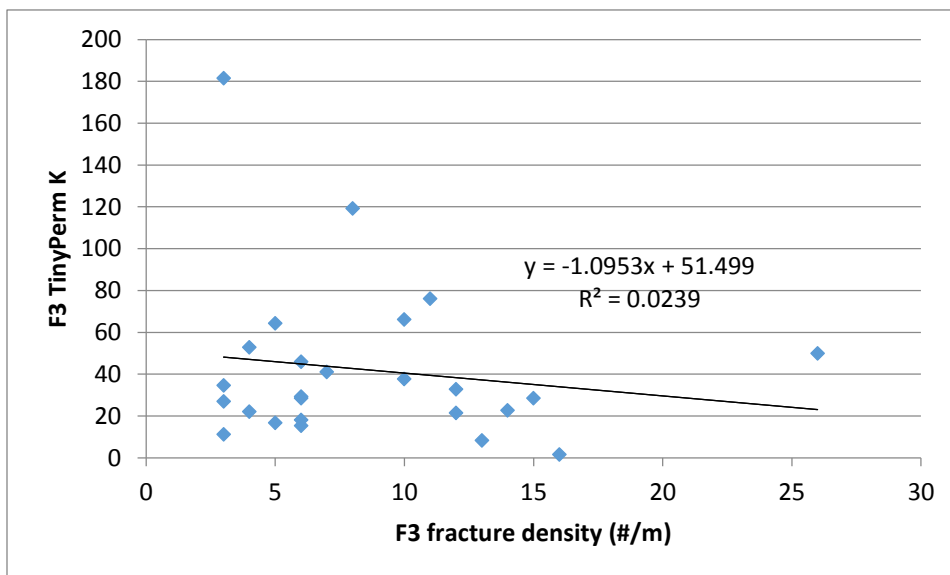

Figure 53. Cross plot of fracture density and permeability data from Fault F3. A negative correlation is shown.

Fracture data from Fault F3 shows an increase in fracture density in the damage

zone from meter 10.5 up to the fault surface at meter 16.5 and then up to mater 22.5 on

the other side of the fault surface. Permeability data looks like it mimics the fracture

density data in places but in other place the trend in the data is very different. The odd

spikes in permeability could be due to error in measurement while using the TinyPerm

tool. These spikes are seen at meter 4.5, 10.5, and 12. At meter 4.5 on the scan line the

point is still in the protolith zone and should have a value between 20 and 40 based on

other samples form the protolith zone on either side of the fault. Permeability at meter

10.5 and meter 12 are more difficult to infer based on the other data. Overall, I conclude

that the permeability data for Fault F3 is unusable due to errors with the TinyPerm tool

causing outliers in the data. The errors come from the tool making a bad seal on the rock

surface due to a failure in the rubber on the end of the tool. A negative correlation of the

permeability and fracture density data can be seen on the cross plot in Figure 53. If we

exclude the outliers in the data there is a general trend in the data (Figure 54). With the

outliers in the data removed fracture density and permeability data correspond with data

from faults F1 and F2.

Thin sections from Fault F3 show evidence of deformation band style faulting.

The fractures present in the thin sections exhibit cataclasis and have been mineralized by

an iron rich fluid. These fractures indicating the proposed first phase of movement can be

seen in Figure 42. Images A, B, and D in Figure 42 all exhibit some degree of cataclasis

and iron oxide mineralization can be viewed in each one. Iron oxide is seen mineralized

in the pore spaces adjacent to the fractures in all of the images in Figure 42. Also in

Figure 42 is an example of an alteration halo boundary in thin section. Image C shows the edge of one of these alteration halos illustrated by a red line. In the area of the alteration halo the pore spaces are filled with what looks like iron oxide, kaolinite, and possibly sparry calcite. The kaolinite could possibly be depositional or the kaolinite could have been emplaced in the pore space as part of the same fluid flow that mobilized the iron oxide and mineralized it in the pore spaces. The kaolinite is likely readily available due to breaking down of microcline feldspar grains in the formation.
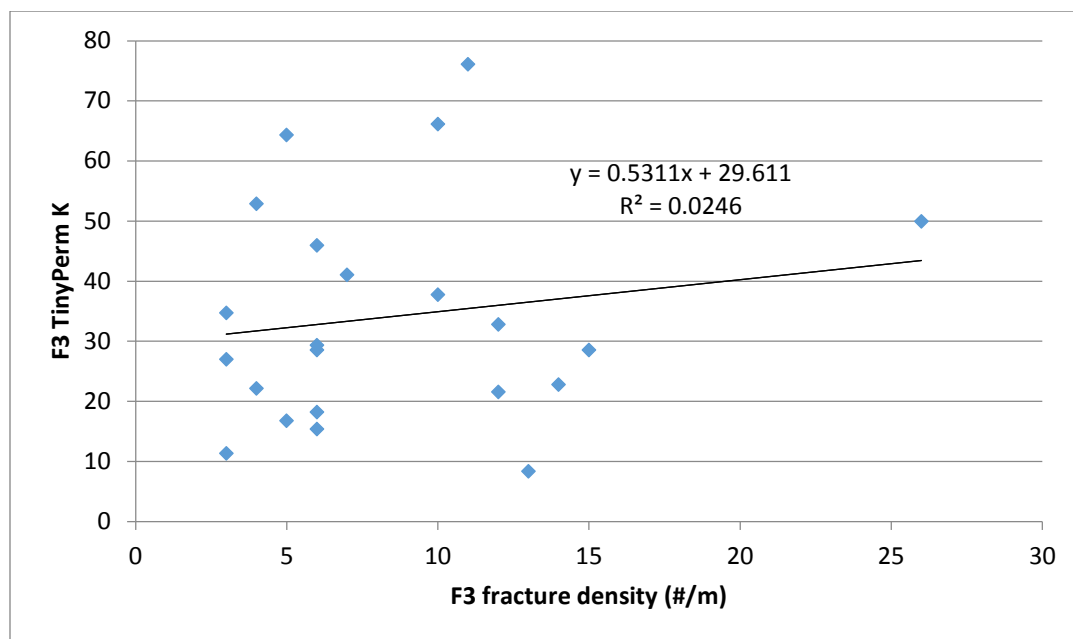

Figure 54. Fracture density and permeability cross plot F3 minus outliers.

In Faults F1, F2, and F3 as well as all of the other faults surveyed in the Hite Field Area there is visual evidence in outcrop scale for fluid flow (Figure 55). In areas adjacent to the fault surface in the overlaying Organ Rock Formation bleaching by a possible reducing fluid has occurred. These discolored areas were often the first evidence of

faulting that I observed in the field while collecting data. In areas where the fracture density was increased in the damage zones there was more discoloration in the overlaying strata adjacent to fault surfaces. After analyzing the data from faults F1, F2, and F3 it can be inferred that in these areas there is increased fracture density which has a corresponding increased permeability that allows for fluid flow which has discolored the overlaying Organ Rock Formation in the fault damage zones. In the data we saw evidence on a micro scale for multiple fluid flow events.

Figure 55. Hite Field Area fluid flow field observations. This image shows discoloration of the Organ Rock Formation where a fault damage zone is present.

CHAPTER V

CONCLUSIONS

We examined 34 small-displacement faults in the Hite Fault Group, southeastern Utah and described and characterize three faults and their associated damages zones. This analysis consists of characterization of fault structure, measurement of damage zone dimensions, fault displacement, fault orientation, fracture density within the damage zone, and degree of iron oxide and calcite mineralization. Based on data and analyses preformed on these faults we are able to describe the structural paragenesis, which allows us to show that grain and bed scale fractures as well as small faults are features by which fluids can migrate preferentially.

We show that the faults experienced two phases of fluid movement, both which are associated with a corresponding fluid flow event. The first phase of movement is associated with deformation band faulting and has a sense of shear which can be inferred from cataclasis. This shear direction caused cataclasis of the grains that can be seen in thin section. The deformation bands from this first phase of movement were mineralized by a fluid rich in iron oxide. The second phase of movement is a time when these faults have been reactivated. During this second phase of movement the associated stress was more extensional which assisted in the development of open mode fractures. Open mode fractures can be seen in the damage zones of the faults in the study area. These open mode fractures acted migration pathways for a calcium rich fluid to move through the damage zones of the faults and precipitate calcite.

Our work has implication for a range of applications. We show that simple assumptions regarding the hydraulic character of deformation band faults as low permeability barriers to flow is not always justified, and depending on the stress history, these faults may act as conduits for fluid migration. These implications directly relate to fluid migration in petroleum reservoirs. Showing that fluids have the ability to migrate preferentially does not only have significance in the petroleum industry but others as well. Another example is in the mining industry where in structurally controlled systems fluids flow preferentially along structures and may result in formation of ore bodies.

REFERENCES

Antonellini, M,. and Aydin, A., 1994, Effect of faulting on fluid flow in porous sandstones: Petrophysical Properties: American Association of Petroleum Geologists Bulletin, v. 78, no. 3, p. 355-377.

Aydin, A., and Johnson, A., 1978, Development of faults as zones of deformation bands and as slip surfaces in sandstone: Pure and Applied Geophysics, v. 116, p. 931-942.

Baars, D. L., and Stevenson, G. M., 1981, Tectonic evolution of western Colorado and eastern Utah, *in* New Mexico Geologic Society, 32nd Annual Field Conference Guidebook, Western Slope, Colorado, p. 105-112.

Barbeau, D. L., 2003, A flexural model for the Paradox Basin: implications for the tectonics of the Ancestral Rocky Mountains: Basin Research, v. 15, no. 1, p. 97-115.

Beitler, B., Parry, W. T., and Chan, M. A., 2005, Fingerprints of the fluid flow: chemical diagenetic history of the Jurassic Navajo Sandstone, Southern Utah, U.S.A.: Journal of Sedimentary Research, v. 75, p. 547-561.

Blakey, R. C., 1996, Permian aeolian deposits, sequences, and sequence boundaries, Colorado Plateau, *in* Sonnenfeld, M.D., and Longman, M.W., eds., Paleozoic systems of the Rocky Mountain Region: Rocky Mountain Section of The Society for Sedimentary Geology, Denver, p. 405-426.

Caine, J. S., Evans, J. P., and Forster, C. B., 1996, Fault zone architecture and permeability structure: Geology, v. 24, p. 1025-1028.

Chan, M. A., Parry, W. T., & Bowman, J. R., 2000, Diagenetic hematite and manganese oxides and fault-related fluid flow in Jurassic sandstones, Southeastern Utah. American Association of Petroleum Geologists Bulletin, v. 84, p. 1281-1310.

Condon, S. M., 1997, Geology of the Pennsylvanian and Permian Cutler Group and Permian Kaibab Limestone in the Paradox Basin, southeastern Utah and southwestern Colorado: Chapter P of Evolution of Sedimentary Basins – Paradox Basin: U.S. Geological Survey Bulletin 2000-P, 44 p.

Davatzes, N. C., Eichhubl, P., and Aydin, A., 2005, Structural evolution of fault zones in sandstone by multiple deformation mechanisms: Moab fault, southeast Utah: Geological Society of America Bulletin, v. 117, no. 1, p. 135-148.

Davis, G. H., 1999, Structural Geology of the Colorado Plateau Region of Southern Utah, with Special Emphasis on Deformation Bands: Geological Society of America Special Paper 342, Boulder, Colorado, 157 p.

Dockrill, B., and Shipton, Z. K., 2010, Structural controls on leakage from a natural CO_2 geologic storage site: Central Utah, U.S.A.: Journal of Structural Geology, v. 32, p. 1768–1782.

Energy Information Administration Report, 2015, Annual Energy Outlook 2015 with projections to 2040: U.S. Energy Information Administration, p. 1-31.

Evans, J. P., and Petrie, E. S., 2012, Analyses of deformation and flow properties in fractured and faulted Permian Cedar Mesa Formation, southeastern Utah [Grant proposal]: Logan, Utah State University, p. 1-12.

Fossen, H., Schultz, R. A., Shipton, Z. K., and Mair, K., 2007, Deformation bands in sandstone: a review: Journal of the Geological Society, v. 164, p.1-15.

Frahme, C. W., and Vaughn, E. B., 1983, Paleozoic geology and seismic stratigraphy of the northern Uncompahgre front, Grand County, Utah, *in* Lowell, J.D., ed., Rocky Mountain foreland basins and uplifts: Rocky Mountain Association of Geologists, p. 201-211.

Goldstrand, P. M, 1994,Tectonic development of Upper Cretaceous to Eocene strata of southwestern Utah: Geological Society of America Bulletin, v. 106, p. 145-154.

Harry, D. L., and Mickus, K. L., 1998, Gravity constraints on lithospheric flexure and the structure of the late Paleozoic Ouachita orogeny in Arkansas and Oklahoma, south-central North America: Tectonics, v. 17, no. 2, p. 187-202.

Huntoon, J. E., Stanesco, J. D., Dubiel, R. F., and Dougan, J., 2003, Geology of Natural Bridges National Monument, Utah, *in* Sprinkel, D.A., Chidsey, T.C., Jr., and Anderson, P.B., eds., Geology of Utah's Parks and Monuments (second edition): Bryce Canyon Natural History Association and Utah Geological Association, v. 28, p. 233-249.

Kelly, V. C. and Clinton, N. J., 1960, Fracture Systems and Tectonic Elements of the Colorado Plateau: University of New Mexico Publications in Geology, no. 4, p. 104.

Kluth, C. F., and Coney, P. J., 1981, Plate tectonics of the Ancestral Rocky Mountains: Geology, v. 9, p. 10-15.

Langford, R., and Chan, M. A., 1988, Flood surfaces and deflation surfaces within the Cutler Formation and Cedar Mesa Sandstone (Permian), southeastern Utah: Geological Society of America Bulletin, v. 100, p. 1541-1549.

Laubach, S. E., Eichhubl, P., Hilgers, S., and Lander, R. H., 2010, Structural diagenesis: Journal of Structural Geology, v. 32, p. 1866-1872.

Loope, D. B., 1984, Aeolian origin of Upper Paleozoic sandstones, southeastern Utah: Journal of Sedimentary Petrology, v. 54, no. 2, p. 563-580.

Mack, G. H., 1978, The survivability of labile light-mineral grains in fluvial, aeolian and littoral marine environments: the Permian Cutler and Cedar Mesa Formations, Moab, Utah: Sedimentology, v. 25, p. 587-604.

MacRae, C. M., and Wilson, N. C., 2008, Luminescence database I-Minerals and Materials, Microscopy and Microanalysis, v. 14, p. 184-204.

Magoon, L., and Dow, W., 1994, The Petroleum system-from source to trap: American Association of Petroleum Geologists Bulletin, v. 60, p. 3-24.

Nelson, R. A., 2001, Geological analysis of naturally fractured reservoirs (second edition): Houston, Texas, Gulf Publishing, 352 p.

Parry, W. T., Chan M. A., and Beitler B., 2004, Chemical bleaching indicates episodes of fluid flow in deformation bands in sandstone: American Association of Petroleum Geologists Bulletin, v. 88, p. 175-191.

Petrie, E. S., Petrie, R. A., and Evans, J. P., 2013, Identification of reactivation and increased permeability associated with a fault damage zone using multidisciplinary approach: Journal of Structural Geology, v. 59, p. 37-49.

Shipton, Z. K., Evans, J. P., Robeson, K. R., Forster, C. B., and Snelgrove, S., 2002, Structural heterogeneity and permeability in faulted aeolian sandstone: Implications for subsurface modeling of faults: American Association of Petroleum Geologists Bulletin, v. 86, no. 5, p. 863-883.

Skurtveit, E., Torabi, A., Alikarame, R., and Braathen, A., 2015, Fault baffle to conduit developments: reactivation and calcite cementation of deformation band fault in Aeolian sandstone: Petroleum Geoscience, v. 21, p. 3-16.

Stanesco, J. D., and Campbell, J. A., 1989, Aeolian and nonaeolian facies of the Lower Permian Cedar Mesa Sandstone Member of the Cutler Formation, southeastern Utah.: U.S. Geological Survey Bulletin 1808-F, 13 p.

Thaden, R. E., Trites, A. F., Jr., Finnell, T. L., and Willis, G.C., 2008, Geologic map of the White Canyon - Good Hope Bay area, Glen Canyon National Recreation Area, Utah: Utah Geological Survey Miscellaneous Publication 08-3DM, scale 1:50,000 (Digitized and modified from U.S. Geological Survey Bulletin 1125, scale 1:48,000, published in 1964).

The National Atlas of the United States of America, 2004, Nationalatlas.gov where we

    are Utah: http://nationalatlas.gov/printable/images/pdf/reference/pagegen_ut.pdf

    (accessed September 2014).

Walsh, P., and Schultz-Ela, D. D., 2003, Mechanics of graben evolution in Canyonlands

    National Park, Utah: Geological Society of America Bulletin, v. 115, no. 3, p.

    259-270.

Willis, G.C., 2012, Geologic map of the Hite Crossing-Lower Dirty Devil River area,

    Glen Canyon National Recreation Area, Garfield and San Juan counties, Utah.

    Utah Geologic Survey Map 254DM, scale 1:62,500, 1 sheet.

APPENDICES

Appendix A: Selected X-ray Diffraction Patterns and Data
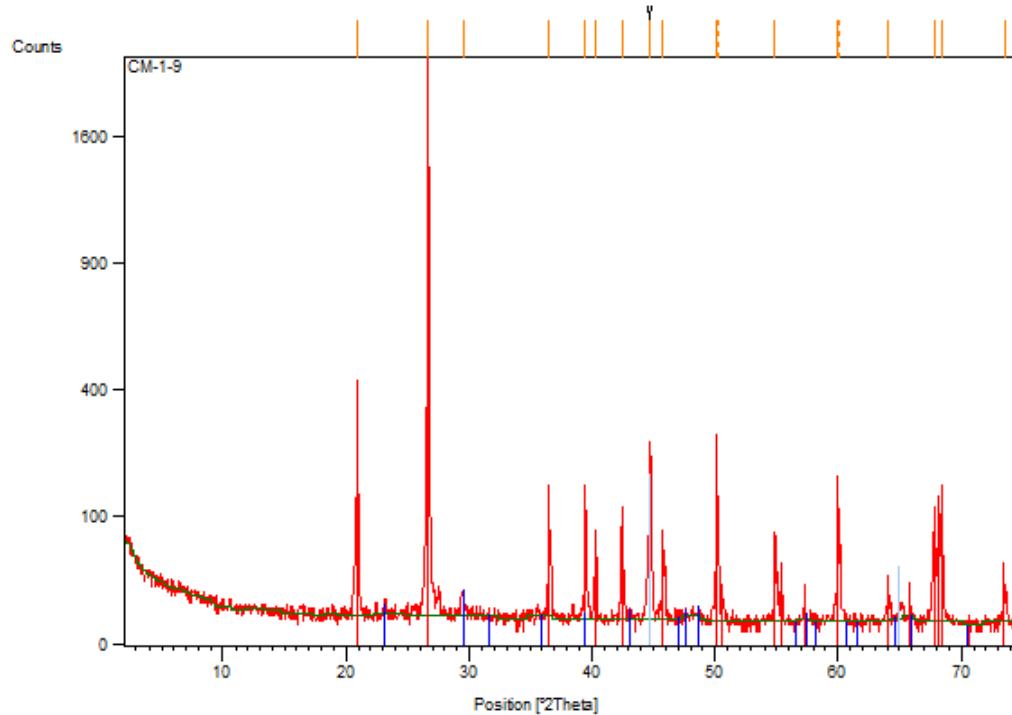
Figure A1. X-ray diffraction pattern from sample at meter 9 on Fault F1 (F1-9). The largest peaks are associated with quartz. The peaks at 29.0 and 38.5 2Θ suggests mineral calcite.
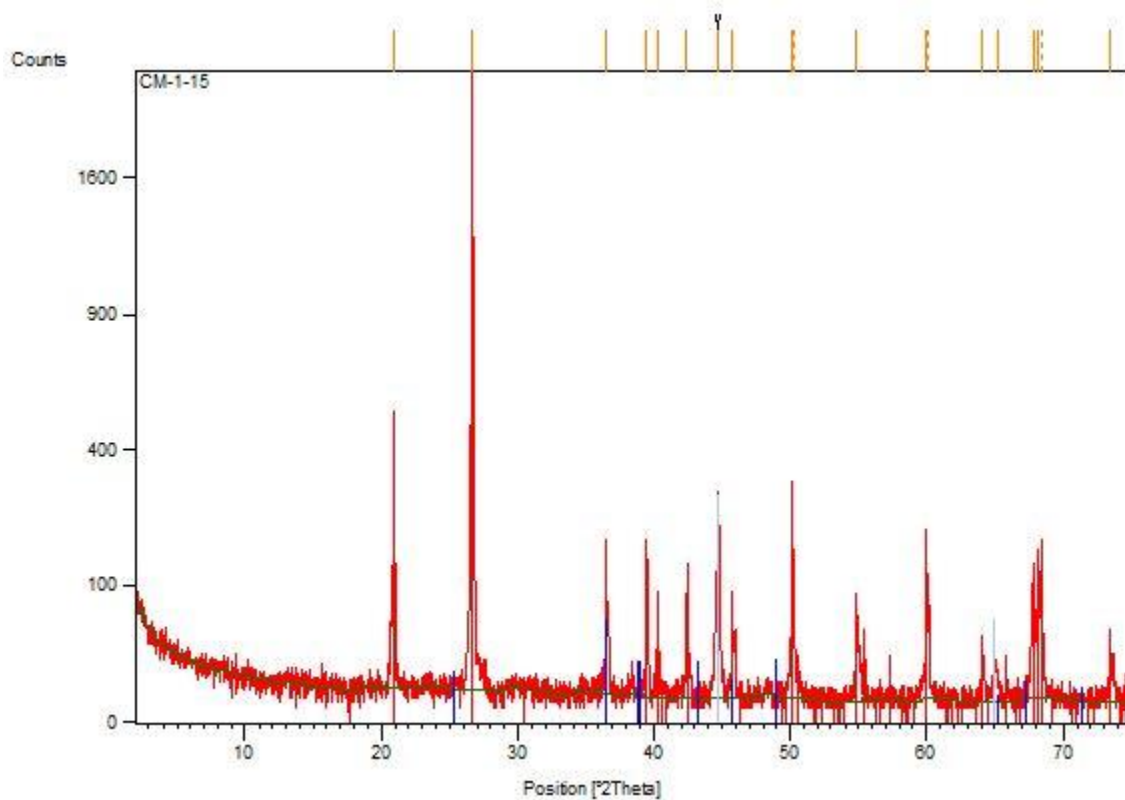
Figure A2. X-ray diffraction pattern from sample at meter 15 on Fault F1 (F1-15). The largest peaks are associated with quartz. The peak at 36.7 2Ө suggests mineral Aragonite.
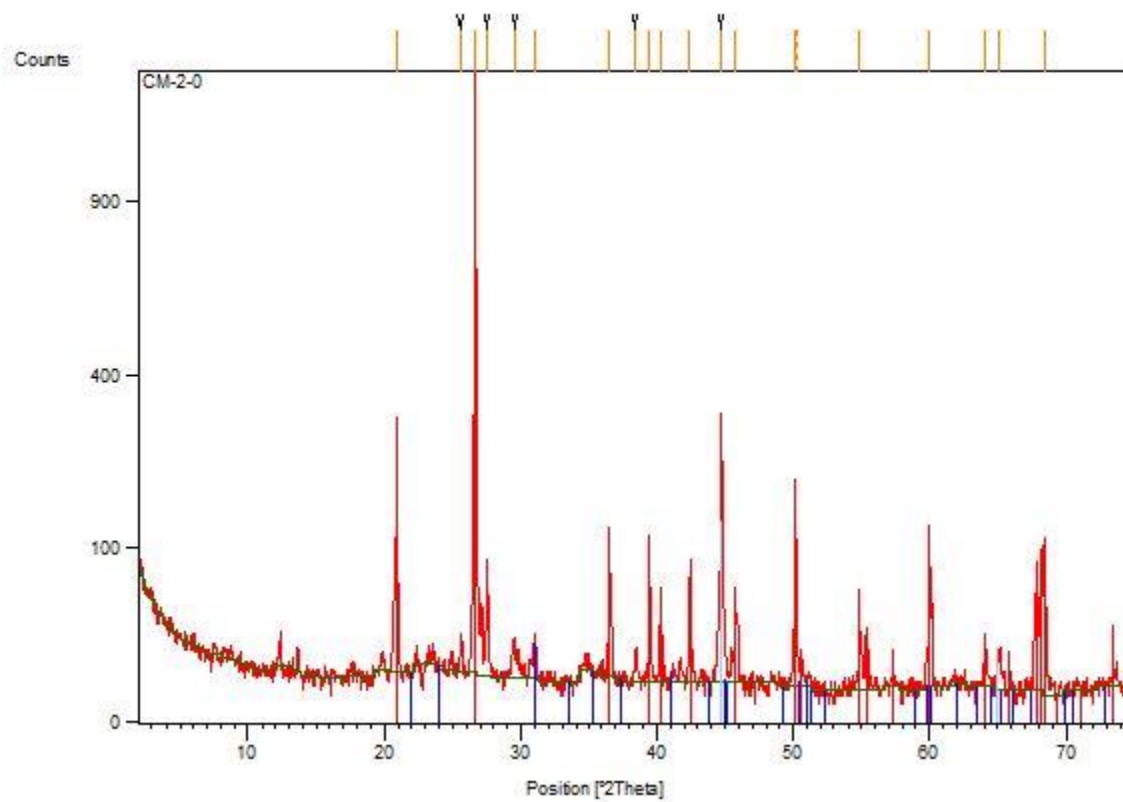
Figure A3. X-ray diffraction pattern from sample at meter 0 on Fault F2 (F2-0). The largest peaks are associated with quartz. The peak at 31.1 2Ө suggests mineral Dolomite.

Appendix B: Whole Thin Section Photographs

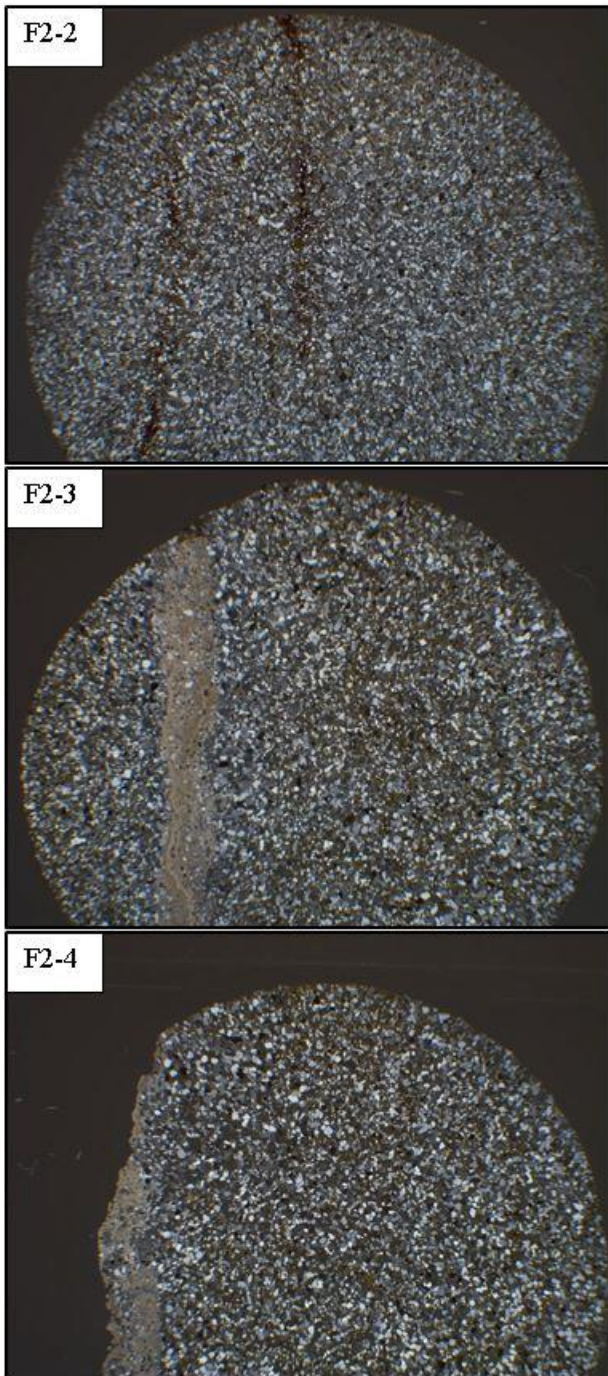Figure A4. Select thin sections photos from meters 0, 12, and 24 along Fault F1.

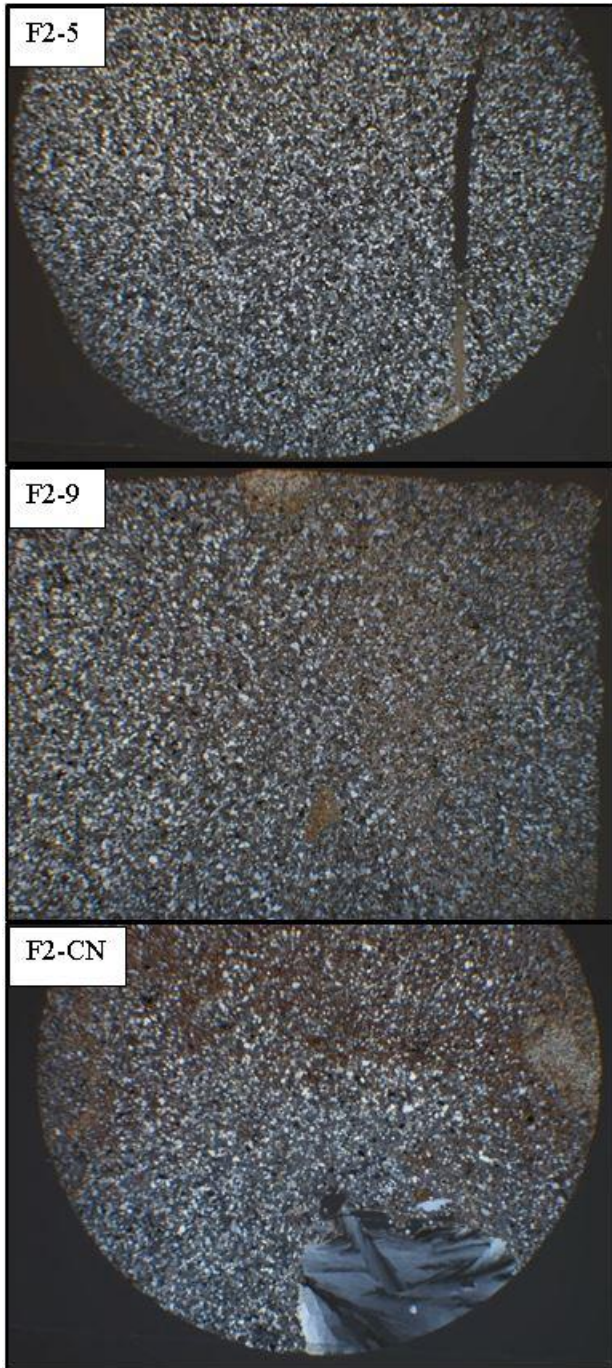Figure A5. Select thin sections photos from meters 2, 3, and 4 along Fault F2.

Figure A6. Additional select thin sections photos from meters 5 and 9 along Fault F2. Also included is a thin section from an area off of the scan line (F2-CN).
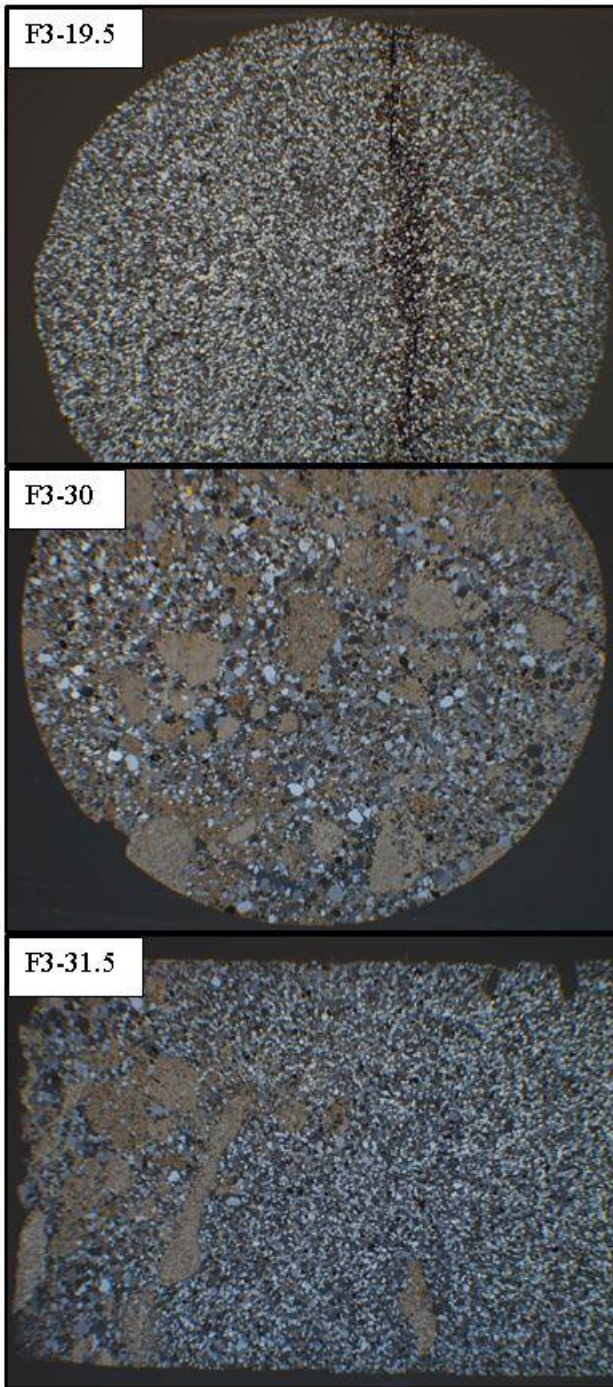
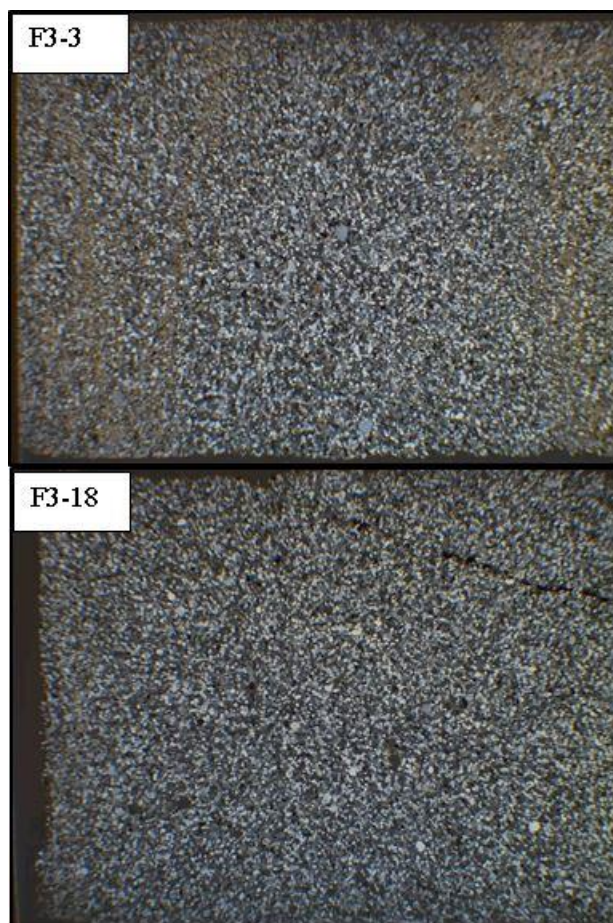Figure A7. Select thin sections photos from meters 19.5, 30, and 31.5 along Fault F3.

Figure A8. Additional select thin sections photos from meters 3 and 18 along Fault F3.